

Interneurons and Amyloid-Beta in Alzheimer's Disease

Arianna Neal

Yale University

Author Note

Arianna Neal, Department of Psychology, Yale University.

This research was supported by Alex Kwan and Farhan Ali of the Kwan Lab, Department of Psychiatry, Yale School of Medicine.

Correspondence should be directed to Arianna Neal, 11401 Maryvale Rd, Upper Marlboro, MD 20772. Contact: arianna.neal@yale.edu.

Abstract

Parvalbumin- (PV) and somatostatin- (SST) positive GABAergic interneurons play powerful roles in cortical networks. However, their relationship to amyloid- β peptide ($A\beta$) and plaque aggregation in Alzheimer's disease (AD) is not well studied. We used immunohistochemical methods to investigate the relationship between PV and SST neurons and $A\beta$ and plaque aggregation in the cingulate 1/secondary motor cortex (Cg1/M2) in tissues from 5XFAD transgenic mice and human patients diagnosed with AD. Areas near PV interneurons exhibited high $A\beta$ and plaque load in human and mouse tissues. However, $A\beta$ and plaque load were low inside PV cells in human and mouse tissues. Areas near SST interneurons exhibited low vulnerability to $A\beta$ and plaques in mouse tissues. Next, given our finding that PV cells are characterized by high plaque load and the finding by Ali, et al. that increased plaque load is correlated with loss of cell density, we attempted to examine how PV interneuron density differs by subtype between chandelier and basket PV cells in 5XFAD mice (n.d.). After several unsuccessful attempts to label PV cells and their respective targets, we identified methods for staining chandelier PV cells and their targets, axon initial segments, and for staining basket PV cells and their targets, neuronal cell bodies, in parallel. Overall, these findings demonstrate that the PV interneuron microenvironment is conducive to aggregation of $A\beta$, thus identifying the PV cell microenvironment as a potential locus for therapeutic intervention.

Keywords: parvalbumin, amyloid- β peptide, Alzheimer's disease, plaques, basket cells, chandelier cells, GABAergic interneurons, 5XFAD

Interneurons and Amyloid-Beta in Alzheimer's Disease

Alzheimer's disease (AD) is a progressive neurodegenerative disorder and the most common cause of dementia; AD is the sixth leading cause of death in the United States, and to date, there is no cure (Masters et al., 2015). AD is neuropathologically characterized by extracellular plaques, which are accumulations of misfolded insoluble amyloid- β protein ($A\beta$), and intracellular tangles, which are formed by fibers of hyperphosphorylated microtubule protein, tau (Masters et al., 2015; Calhoun et al., 1998).

Familial Alzheimer's disease (FAD) is a subtype of AD that is caused by mutations in the gene for amyloid precursor protein (APP), the protein from which $A\beta$ is cleaved, and the genes for presenilin 1 (PS1) and presenilin 2 (PS2). PS1 and PS2 are subunits of γ -secretase, one family of enzymes responsible for proteolytically cleaving APP (Oakley et al., 2006). These mutations in the genes for APP, PS1, and PS2 cause the overproduction and incorrect cleavage of $A\beta$, followed by the deposition of this misfolded $A\beta$ outside of the cell (Masters et al., 2015).

Vulnerability to deposition of insoluble miscleaved and misfolded $A\beta$ differs significantly by cortical region. Studies of patterns of amyloid deposition in postmortem brain tissue samples from AD patients have demonstrated that the cortical regions most vulnerable to amyloid plaque formation are the higher-order association cortices (Arnold, Hyman, Flory, Damasio, & Van Hoesen, 1991). Such histopathological studies have also demonstrated that degeneration occurs most markedly in the medial temporal and frontal lobes, with primary motor and sensory cortices experiencing degeneration

only in late stages of disease progression (Brun & Englund, 1981). These observed deposition patterns are consistent with findings of positron emission tomography imaging of amyloid deposition in the cortices of living patients diagnosed with AD (Klunk et al., 2004; Rowe et al., 2007). So, in AD patients, misfolded A β is deposited most abundantly in the higher-order association cortices, while sensorimotor cortices are left comparatively healthy until very late-stage AD.

A β deposition occurs differentially not only by cortical region, but also by cortical layer and morphological species of A β . Morphology of A β can often be categorized into one of three categories: diffuse deposits, primitive deposits, and classic deposits (Armstrong, 2015). Diffuse deposits have not yet formed β -pleated fibrils, dystrophic neurites, or helical filaments, while primitive deposits are characterized by the presence of each of those three structures (Armstrong, 2015). Classic deposits are densely packed amyloid cores surrounded by rings of dystrophic neurites (Armstrong, 2015). Histopathological studies of tissues obtained from AD patients demonstrate that diffuse and primitive deposits are found most abundantly in the upper cortical layers, while classic deposits are often found more frequently in the lower cortical layers (Armstrong, 2015).

Once deposited extracellularly, insoluble, misfolded A β deposits aggregate into the cortical plaques characteristically observed in AD neuropathology. Histopathological studies of postmortem brain tissue samples from human AD patients have found that aggregation of these cortical plaques is positively correlated with cell loss and neural atrophy (Mann, 1985; Cras 1991; Arendt, Bigl, Tennstedt, & Arendt, 1985). While it is

not known exactly how plaques are involved in cell death in AD, major hypotheses include the following: that the miscleaved A β within plaques is directly toxic to neighboring neurons; that the extracellular A β oligomers trigger neuronal death before plaque formation; that cell death is triggered during incorrect processing of APP; and that A β plaques are not a cause of cell death, but rather a byproduct of neurodegeneration (Carter & Lippa, 2001). Thus, plaque aggregation plays a central role in AD pathology, although the mechanisms linking plaques to cell death are unknown.

Of particular interest in the present research is how A β neuropathology is related to alterations in interneuron density and function. Most interneurons are inhibitory GABAergic interneurons, which regulate the activity and synaptic signaling of excitatory pyramidal neurons. In AD, however, several postmortem tissue studies have demonstrated that GABA concentrations are decreased in the temporal, occipital, and parietal lobes, and, in some cases, depleted in the orbitofrontal and premotor regions of the frontal cortex (Govindpani et al., 2017). Other studies of postmortem brain tissues from AD patients have observed reduced density in GABA receptors, damage to GABAergic neuron terminals, and disruption in GABAergic synaptic function (Govindpani et al., 2017). These findings suggest that GABAergic interneuron structure and function are adversely altered during AD disease progression.

Mechanisms of neurodegeneration characteristic of FAD, including A β deposition, plaque aggregation, and alterations to GABAergic interneuron structure and function, can be studied by modeling FAD within transgenic mouse lines. FAD can be

modeled in transgenic mice by overexpressing the mutations that cause amyloid plaque formation (Calhoun et al., 1998). 5XFAD mice are transgenic mice that express five mutations associated with FAD, including three mutations in the gene for APP and two mutations in the gene for PS1, which cause increased production of amyloid- β 42 (A β 42) (Oakley et al., 2006). A β 42 is the 42-amino acid form of incorrectly cleaved A β , which rapidly accumulates into extracellular plaques that cause neurotoxicity, synaptotoxicity, and oxidative stress in transgenic mice models (Oakley et al., 2006; Eimer & Vassar, 2013; Saiz-Sanchez, Ubeda-Banon, De la Rosa-Prieto, & Martinez-Marcos, 2012). 5XFAD mice are useful models for studying human FAD because the brains of 5XFAD mice demonstrate an elevated ratio of A β 42 to A β 40, as observed in human FAD. 5XFAD mice also model working memory deficits, impairments in motor function, and axonal degeneration, as observed in human FAD (Jawhar, Trawicka, Jenneckens, Bayer, & Wirths, 2012; Girard et al., 2013). So, 5XFAD mice are particularly useful because they model A β 42 deposition, plaque aggregation, and cognitive impairments that unfold via processes that may be analogous to those that underlie human FAD.

It is important to note, however, that processes of 5XFAD and human FAD neurodegeneration are not identical. In 5XFAD mice, the elevated A β 42 to A β 40 ratio is higher than in humans, and no human cases of FAD are caused by multiple FAD mutations, as in the case of 5XFAD (Oakley et al., 2006). Furthermore, while 5XFAD mice do model amyloid plaques, they do not exhibit the neurofibrillary tangles also found in human FAD (Oakley et al., 2006). So, while 5XFAD mice do aid the study of

mechanisms potentially analogous to those that underlie human FAD neuropathology and behavioral impairment (Spires & Hyman, 2005), it is crucial that findings of studies in 5XFAD mice are validated by findings of studies of human brain tissue.

Transgenic mice have been used to study the effects of FAD pathology on interneuron structure and function. Two specific types of GABAergic interneurons that have been studied within mice tissues are parvalbumin- and somatostatin-positive neurons. These neurons can be identified by their expression of parvalbumin (PV), a calcium binding protein, or somatostatin (SST), a growth hormone-inhibiting hormone, by immunohistochemical methods in mice tissues (Takahashi et al., 2010; Martinez, 2013; Molgaard et al., 2014). Such transgenic mice studies have observed loss of both PV and SST interneuron density correlated with increased A β , with greater vulnerability to cell death observed in SST interneurons when compared to PV interneurons (Takahashi et al., 2010; Saiz-Sanchez et al., 2012). However, what remains of interest is how patterns of plaque and A β peptide distribution in relation to PV interneurons compare to plaque and A β peptide distribution in relation to SST interneurons in tissues obtained particularly from 5XFAD mice models. Also of interest is how A β deposition alters PV interneuron density, as well as how that relationship is altered by PV interneuron subtype, as examined in tissues obtained from 5XFAD mice models. Such questions can be addressed by staining for A β and plaques while also staining for PV and SST in tissues from 5XFAD mice; in doing so, it is possible to simultaneously assess A β and plaque distribution in relation to PV and SST neurons and PV cell density within cortical tissues from 5XFAD mice.

Hence, the purpose of this research will be to investigate patterns in A β or amyloid plaque distribution in relation to PV or SST interneurons and to examine PV interneuron density by subtype. In the first study, we will use immunohistochemical methods within tissue obtained from 5XFAD mouse models and postmortem tissue samples from human AD patients, and in the second study we will use immunohistochemical methods within 5XFAD tissue only, thus creating a better understanding of the interactions between extracellular A β deposition, plaque load, interneuron type, and interneuron density.

Chapter One: PV Interneurons Possess

Microenvironments Conducive to Accumulation of Amyloid- β

Introduction

Parvalbumin (PV) and somatostatin (SST) interneurons are integral to the GABAergic inhibitory regulation of the activity and synaptic function of pyramidal excitatory neurons. Postmortem studies of brain tissues obtained from human AD patients have demonstrated that SST cells are more colocalized with plaques than PV cells (Saiz-Sanchez, 2015). While it is not yet known how colocalization with amyloid plaques may cause decay in local interneuron structure and function, it is hypothesized that extracellular A β oligomers may trigger local neuronal death, or that the A β within extracellular plaques may be directly toxic to neighboring neurons (Carter & Lippa, 2001). Colocalization of PV and SST interneurons with A β may thus cause interneuron dysfunction and interfere with proper pyramidal neuron regulation in human FAD, although the mechanisms by which this may happen are unknown.

The purpose of the present research is to investigate, using immunohistochemical staining in 5XFAD mouse tissue and postmortem brain tissue from human AD patients with antibodies and dyes targeting PV, SST, all neurons, and A β peptides and plaques, how distribution of A β and plaque load varies in relation to proximity to PV and SST cells when compared to one another and to all other neurons.

Materials and Methods

Animals

5XFAD mice were obtained from Jackson Laboratory (Stock No. 006554, also called MMRRRC Stock No. 34840-JAX). 5XFAD mice overexpress transgenes with five familial Alzheimer's disease (FAD) mutations under the mouse Thy1 promoter, including M146L and L286V mutations in human presenilin-1 and K670N/M671, I716V, and V717I mutations in human amyloid precursor protein (APP). Male 5XFAD mice were mated with female WT mice (C57BL/6J WT strain from Jackson Laboratory, Stock No. 000664) to produce 5XFAD and WT littermates. From these litters, male 5XFAD mice and male wild type (WT) littermate controls aged 6-9 months were used in this experiment. Genotypes were confirmed by polymerase chain reaction. This age range was selected due to the high levels of amyloid- β (A β) known to be present in the mouse cortex at this point in the progression of FAD-like neuropathology in 5XFAD mice (Oakley et al., 2006). Procedures were approved by the Yale University Institutional Animal Care and Use Committee.

Human Postmortem AD Tissue

Postmortem tissue samples from AD-diagnosed patients were obtained from Dr. Jaime Grutzendler at Yale University. Samples were taken from the frontal cortices of the brain.

Immunohistochemistry

Mice were sacrificed and perfused transcardially with phosphate buffered saline (PBS) and then 4% paraformaldehyde (PFA). After harvesting, brains were stored for at least 48 hours in PFA at 4°C. Brains were then transferred from PFA to PBS for storage until slicing. A vibratome was used to slice each brain into 100 µm-thick coronal sections containing the cingulate (Cg1 and Cg2) and secondary motor cortex (M2). Slices were then subjected to free-floating staining as follows.

Plaque and PV staining on mouse tissue. Slices from mouse tissue were incubated for 1 hour in blocking solution (0.5% Triton and 5% goat serum in PBS) at room temperature. Slices were washed three times in PBS and incubated overnight for at least 12 hours in primary polyclonal rabbit anti-PV antibody (Abcam ab11427, 1:1000 dilution in blocking solution) at 4°C. Slices were washed three times in PBS again and then incubated for 3 hours in secondary antibody (goat anti-rabbit IgG H&L Alexa Fluor 555, Abcam ab150078, 1:500 dilution in blocking solution) at room temperature. Slices were washed three times in PBS once more before incubating for 30 minutes in FSB (1:3000 dilution from 5 mg/ml stock, 344101, MilliporeSigma) at room temperature. Slices were washed again in PBS three times and then incubated for 10 minutes in distilled water at room temperature before mounting onto slides. Slides were dried in the dark for at least two hours at room temperature or overnight at 4°C. After drying, slides were coverslipped with DPX mounting medium (06522, MilliporeSigma). Coverslipped slides were dried and stored for long term usage in slide boxes at 4°C.

Plaque and SST staining on mouse tissue. Slices of mouse tissue were incubated for 45 minutes in citrate buffer (1x sodium citrate buffer and 0.05% tween-20 with pH set to 6) at 95°C. After cooling for five minutes at room temperature, slices were washed three times in PBS and incubated for 1 hour in blocking solution (0.5% Triton and 5% goat serum in PBS) at room temperature. Slices were incubated overnight for at least 12 hours in rat anti-SST monoclonal primary antibody (Sigma-Aldrich MAB354, 1:100 dilution) at 4°C. Slices were washed three times in PBS and then incubated for 3 hours in secondary antibody (goat anti-rat IgG H&L Alexa Fluor 555, Abcam ab150158, 1:500 dilution in blocking solution) at room temperature. Slices were washed three times in PBS before incubating for 30 minutes in FSB (1:3000 dilution from 5 mg/ml stock, 344101, MilliporeSigma) at room temperature. Slices were washed again in PBS three times and incubated for 10 minutes in distilled water at room temperature before mounting onto slides. Slides were dried in the dark for at least two hours at room temperature or overnight at 4°C. After drying, slides were coverslipped with DPX mounting medium (06522, MilliporeSigma). Coverslipped slides were dried and stored for long term usage in slide boxes at 4°C.

Plaque and neuronal nuclei (NeuN) staining on mouse tissue. Slices from mouse tissue were incubated for 1 hour in blocking solution (0.5% Triton and 5% goat serum in PBS) at room temperature. Slices were incubated overnight for at least 12 hours in primary monoclonal rabbit anti-NeuN antibody (rabbit monoclonal [EPR12763] to NeuN, Abcam ab177487, 1:500 dilution) at 4°C. Slices were washed three times in PBS again and then incubated for 3 hours in secondary antibody (goat anti-rabbit IgG H&L Alexa Fluor

555, Abcam ab150078, 1:500 dilution in blocking solution) at room temperature. Slices were washed three times in PBS before incubating for 30 minutes in FSB (1:3000 dilution from 5 mg/ml stock, 344101, MilliporeSigma) at room temperature. Slices were washed again in PBS three times and incubated for 10 minutes in distilled water at room temperature before mounting onto slides. Slides were dried in the dark for at least two hours at room temperature or overnight at 4°C. After drying, slides were coverslipped with DPX mounting medium (06522, MilliporeSigma). Coverslipped slides were dried and stored for long term usage in slide boxes at 4°C.

A β and PV staining on mouse and human tissue. Slices of human and mouse tissue were incubated for 45 minutes in citrate buffer (1x sodium citrate buffer and 0.05% tween-20 with pH set to 6) at 95°C. After cooling for five minutes at room temperature, slices were incubated for 20 minutes in 88% formic acid at room temperature. Slices were washed three times in PBS and incubated for 1 hour in blocking solution (0.5% Triton and 5% goat serum in PBS) at room temperature. Slices were washed three times in PBS again and incubated overnight for at least 12 hours in mixed primary antibodies containing polyclonal rabbit anti-PV antibody (Abcam ab11427, 1:500 final dilution) and polyclonal mouse anti-A β antibody (Biolegend 4G8 800712, 1:250 final dilution) at 4°C. Slices were washed three times in PBS and then incubated for 4 hours in mixed secondary antibodies containing goat anti-rabbit antibody (preabsorbed against mouse IgG, Alexa Fluor 555, Abcam ab150086, 1:500 final dilution) and goat anti-mouse antibody (preabsorbed against rabbit IgG, Alexa Fluor 495, Abcam ab150117, 1:200 final dilution) at room temperature. Slices were washed in PBS again

three times, incubated for 10 minutes in distilled water at room temperature, and mounted onto slides. Slides were dried in the dark for at least two hours at room temperature or overnight at 4°C. After drying, slides were coverslipped with DPX mounting medium (06522, MilliporeSigma). Coverslipped slides were dried and stored for long term usage in slide boxes at 4°C.

Imaging

We used a confocal laser scanning microscope (Olympus FV1000) and its accompanying software for all imaging. Under widefield fluorescence mode, we first identified the frontal regions (Cingulate 1, Cg1, and secondary motor area, M2) to be imaged using landmarks such as white matter and ventricles. After delineating the area to be imaged, the lasers for neuronal (PV or SST or NeuN) (559 nm), plaque (405 nm), or A β (473 nm) staining were turned on for confocal imaging. We took nonoverlapping images (800 x 800 pixels/image, 0.265 μ m/pixel) at random locations in Cg1 and M2 using a 20x objective with a focal plane at approximately 10 μ m deep into the brain section.

Analysis – Plaques and amyloid- β ROIs

The first step involved manual identification of plaques based on morphology and brightness of fluorescent signals compared to background (**Figure 1.1B**, left). A region of interest (ROI) encompassing each identified amyloid- β plaque was manually drawn using the freehand selection tool in ImageJ. This hand-drawn ROI was made to trace

the most exterior perimeter of the plaque structure, keeping in mind that the second step would refine and classify the pixels in a more unbiased, automated manner. For the second step, the hand-drawn ROIs (**Figure 1.1B**, middle) along with the original fluorescence image were imported into MATLAB (Mathworks). For each plaque, a background ROI was estimated by calculating r , the radius of a circle if the hand-drawn ROI area was considered as the area of a circle, and then creating a background ROI which was a circle with a radius of $3r$, excluding pixels belonging to the hand-drawn ROI itself as well as overlapping hand-drawn ROIs of other nearby plaques. A threshold was calculated as two times the standard deviation above the mean of values of all the pixels within the background ROI. From the hand-drawn ROI, pixels above the threshold were kept to generate the final ROI for a plaque (**Figure 1.1B**, right). This process was repeated for all of the plaques identified in the first step. This two-step procedure for analyzing plaques provides a consistent way to compute plaque area, taking into account local differences in background fluorescence (for example, due to nonuniform staining) and reduces human bias. We performed the same procedures for identifying amyloid- β labeled by 4G8 antibody. We additionally differentiated between extracellular and intracellular amyloid- β (see **Figures 1.5A** and **1.6A** for examples).

Analysis – Neuron ROIs

For PV and SST neuronal staining, we manually drew ROIs using the freehand selection tool in ImageJ. For NeuN neuronal staining, because there were typically over one hundred NeuN-positive neurons in each image, we performed a two-step

procedure. First, we used an automated segmentation procedure in CellProfiler. This selected 80-90% of the NeuN-positive neurons. The rest of the neurons were manually drawn using the freehand selection tool in ImageJ. We used Matlab to then combine these ROIs from different steps. All neuron ROIs were drawn blind to the 2nd channel (plaques or amyloid- β) data.

Analysis – Combined

All ROIs were subsequently imported into Matlab for further analysis. To quantify plaque load, we drew ring-like masks of radii 0-10 μm , 11-20 μm , 21 – 50 μm and 51 – 100 μm from the boundary of the neuron. Pixels positive for plaque or amyloid- β were summed and divided by the total number of pixels in each of the masks to produce a measure of plaque load. Relative plaque load was then obtained by dividing this number by the overall plaque load for the whole 800 x 800 pixel image (212 x 212 μm) (sum of all pixels positive for plaque or amyloid- β divided by 800 x 800 pixels). This normalization allowed us to then combine the datasets from different images and animals/patients with different extent of plaque/ amyloid- β deposits. Our relative plaque load measure thus quantifies the fold increase (or decrease) of plaque or amyloid- β deposits in different areas around a neuron compared to the overall plaque load regardless of presence/absence of neurons. To generate the images showing probability and intensity of plaques or amyloid- β , we first segmented a 200 x 200 μm image with center at the centroid of the neuron (computed by 'regionprops' function in Matlab). We then noted the distribution of plaques or amyloid- β . Pixels in the 200 x 200 μm image that were

outside the original image were set to 'NaN'. We did this procedure for all neurons for all the datasets. To obtain the probability of plaques or amyloid- β , for each pixel, we divided the number of plaque or amyloid- β -positive pixels from all the images by the number of non-NaN pixels. To obtain the mean plaque or amyloid- β -positive intensity, for each pixel, we took the mean from all images, ignoring pixels with NaN entries. These procedures are equivalent to z-projections (z being the axis of the number of images). For statistical comparisons, we used parametric paired-sample t-test (two-tailed with $\alpha = 0.05$).

Results

We stained, imaged, and analyzed plaques, PV neurons, SST neurons, NeuN-positive neurons, extracellular A β , and intracellular A β in the cingulate 1/secondary motor (Cg1/M2) cortical regions of brain tissue obtained from 5XFAD mice. We also stained, imaged, and analyzed A β and PV neurons in postmortem brain tissue obtained from human AD patients.

The tissue imaged in the Cg1/M2 is labeled in **Figure 1.1A**; examples of ROI drawing for A β plaques and PV neurons are illustrated in **Figures 1.1B** and **1.1C**, respectively.

Using tissue from 5XFAD mice, we first imaged plaques and PV neurons in separate channels and then merged these channels to produce overlapping composite images of both PV and plaques (**Figure 1.2A**). We used these composite images to generate boxplots of relative plaque load as a function of distance to the boundary of

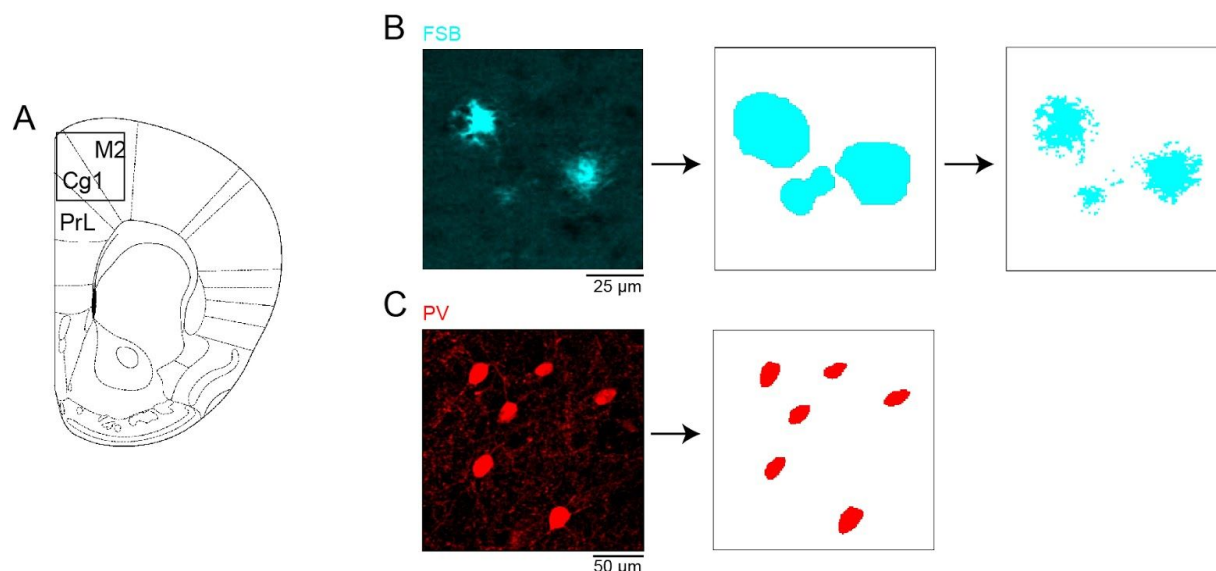


Figure 1.1. Selection of plaque and PV neuron ROIs in Cg1/M2 region of neocortex.

(A) Coronal section of the cingulate cortex (Cg1) and secondary motor cortex (M2) regions examined in this study, according to a brain atlas by Paxinos and Franklin (2012).

(B) Left: example of amyloid- β plaques stained by FSB. Center: corresponding ROIs drawn manually for each amyloid- β plaque. Right: final ROIs for amyloid- β plaques according to local thresholding procedures. See Materials and Methods for details.

(C) Left: example of PV neurons stained by anti-PV antibodies. Right: corresponding ROIs drawn manually for each PV neuron.

the neuron (**Figure 1.2B**), where relative plaque load is the fold difference relative to overall plaque load of each field of view. Mean relative plaque load was increased the most at distances of 0-10 μm and 11-20 μm to the neuron, where mean plaque load was increased by 30% and 43%, respectively. At distances of 21-50 μm and 51-100 μm , mean plaque load was increased by 12% and 7%. Paired sample t-tests between 0-10 μm , 11-20 μm , or 21-50 μm and 51-100 μm revealed that changes in relative plaque load were significant at 0-10 μm and 11-20 μm , but not 21-50 μm when compared to 51-100 μm . Next, we collapsed composite images into single plots of

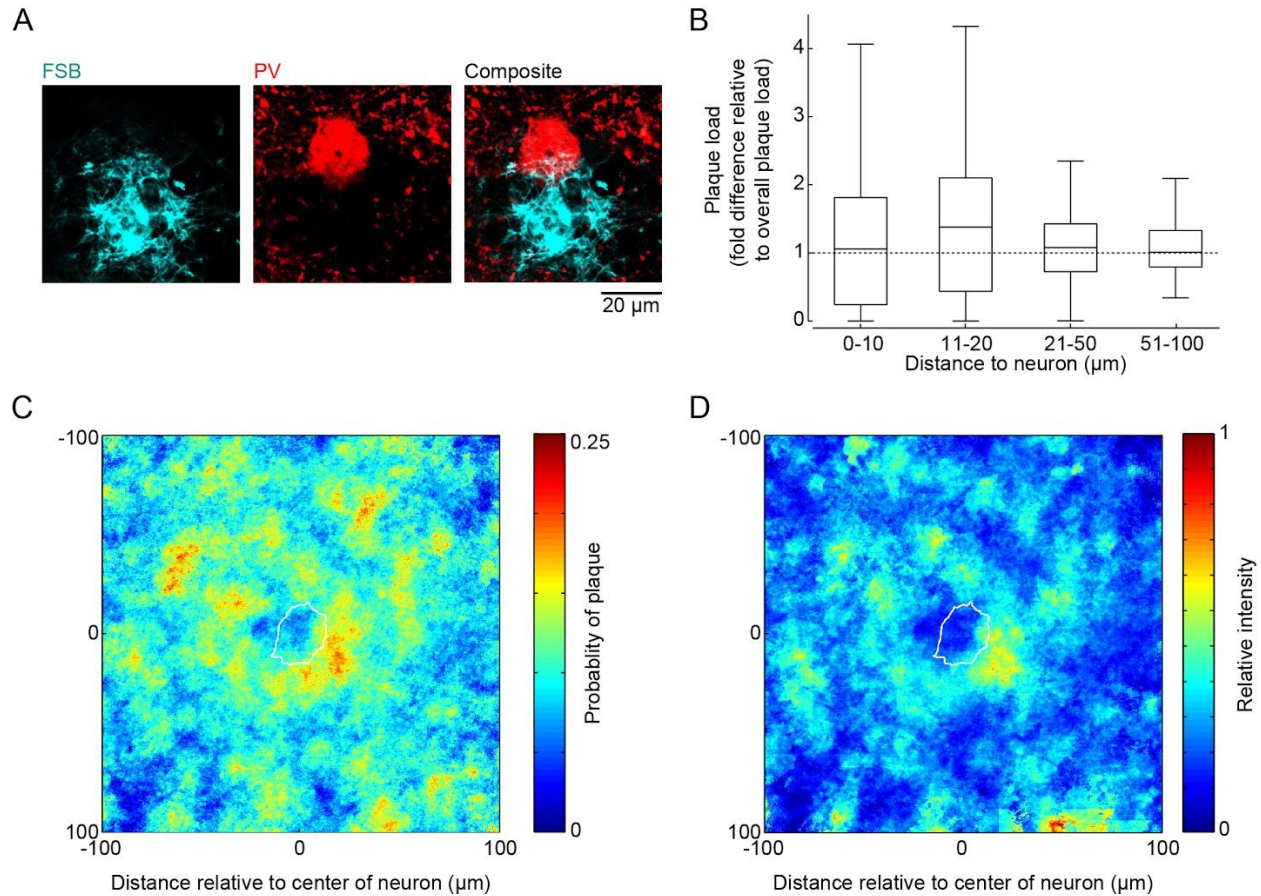


Figure 1.2. Plaques and PV neurons in 5XFAD mice.

(A) Example FSB staining of plaques (left), PV neuron (middle) and composite (right).

(B) Boxplot (median, 25th percentile, 75th percentile and ± 1.5 IQR from 25th and 75th percentile respectively) of plaque load as a function of distance from boundary of neuron. Plaque load is quantified as fold difference relative to the overall plaque load of each field of view. See Methods for details. Relative plaque load (mean \pm SEM): 1.30 ± 0.10 , 0-10 μm ; 1.43 ± 0.08 , 11-20 μm ; 1.12 ± 0.04 , 21 - 50 μm ; 1.07 ± 0.03 , 51-100 μm . Paired sample t-tests indicated a significant difference between relative plaque load at 0-10 ($p = 0.048$) μm and 11-20 μm ($p = 7 \times 10^{-4}$) but not 21 - 50 μm ($p = 0.46$) compared to 51-100 μm . $n = 183$ neurons, 7 animals.

(C) Probability of plaque as a function of distance relative to center of PV neuron. Outline from the boundary of an "average" neuron overlaid. Note the increased probability of finding plaques near and around PV neurons.

(D) Relative FSB staining intensity as a function of distance relative to center of PV neuron. Outline from the boundary of an "average" neuron overlaid. Note the increased intensity of FSB staining in areas near and around PV neurons.

probability of plaque versus distance to an “average” PV neuron’s center (**Figure 1.2C**) and relative intensity of plaque staining versus distance to an “average” PV neuron’s center (**Figure 1.2D**) (see methods for details). The probability of finding a plaque and relative intensity of plaque staining appeared to be low at the PV neuron’s center and high in the PV neuron’s local environment.

After staining, imaging, and analyzing plaques and PV neurons in 5XFAD mice tissue, we imaged and analyzed plaques and SST neurons in 5XFAD mice tissue. Again, we produced composite images of plaque and SST staining (**Figure 1.3A**) and used those composite images to make boxplots of relative plaque load as a function of distance from the boundary of the SST neuron (**Figure 1.3B**). Here, mean relative plaque load was decreased by 32% at 0-10 μm , while mean relative plaque load was increased by 14% at 11-20 μm , 7% at 21-50 μm , and 18% at 51-100 μm . Median relative plaque load was decreased at all distances except 51-100 μm . Paired sample t-tests revealed significant difference in relative plaque load at 0-10 μm , but not 11-20 μm or 21-50 μm , when compared to plaque load at 51-100 μm . The probability of finding a plaque and relative intensity of plaque staining were overall much lower near and around SST neurons (**Figures 1.3C** and **1.3D**) than around PV neurons (**Figures 1.2C** and **1.2D**).

We next imaged and analyzed plaques and NeuN-positive neurons in 5XFAD mice tissue, again creating composite images from merged images of plaque and neuronal nuclei staining (**Figure 1.4A**) to generate boxplots of relative plaque load as a

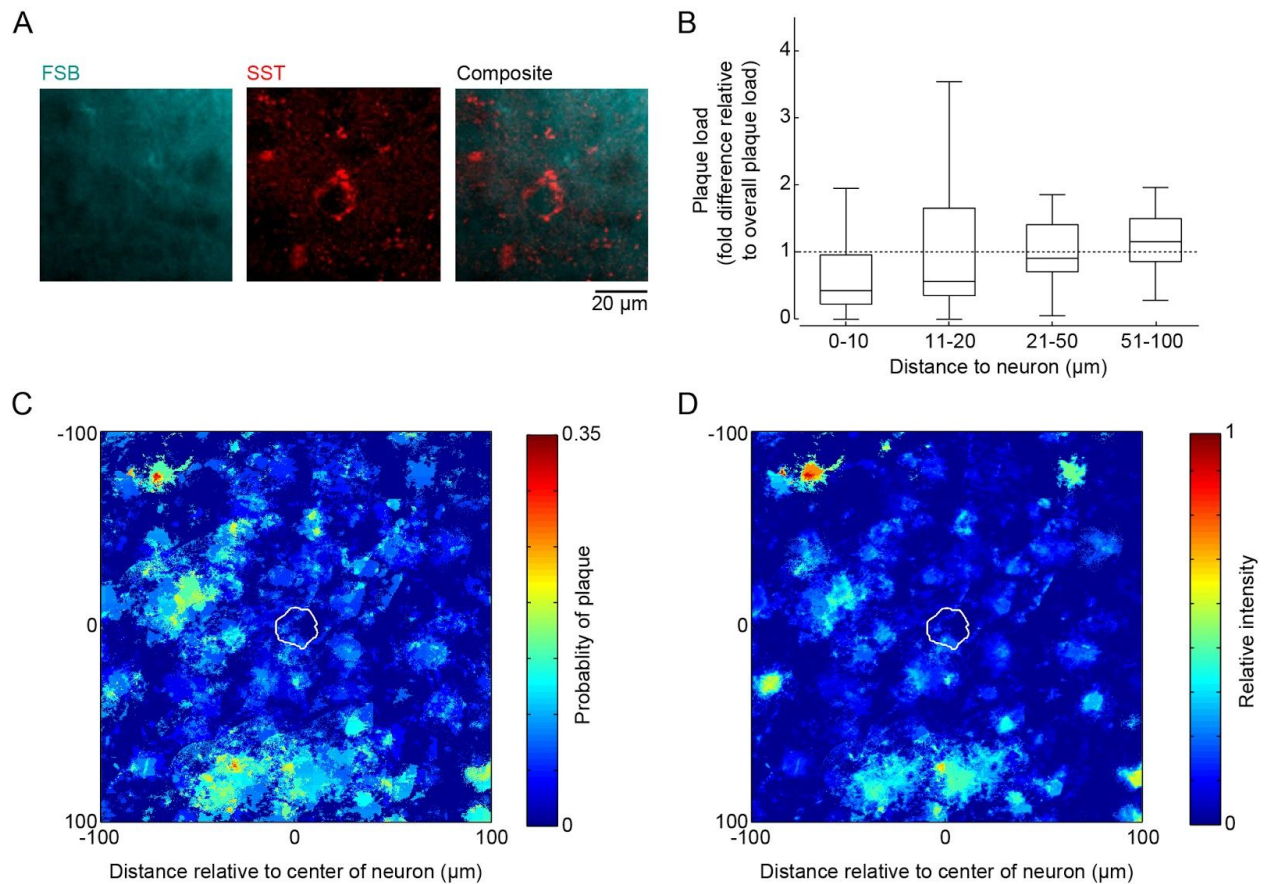


Figure 1.3. Plaques and SST neurons in 5XFAD mice.

(A) Example FSB staining of plaques (left), SST neuron (middle) and composite (right).
 (B) Same as Figure 2B but for SST neurons. Relative plaque load (mean \pm SEM): 0.68 ± 0.14 , 0-10 μm ; 1.14 ± 0.22 , 11-20 μm ; 1.07 ± 0.10 , 21 - 50 μm ; 1.18 ± 0.07 , 51-100 μm . Paired sample t-tests indicated a significant difference between relative plaque load at 0-10 μm ($p = 0.004$) μm but not 10 - 20 μm ($p = 0.89$) or 21 - 50 μm ($p = 0.43$) compared to 51-100 μm . $n = 38$ neurons, 5 animals.
 (C) Same as Figure 1.2C but for SST neurons.
 (D) Same as Figure 1.2D but for SST neuron.

function of distance to the boundary of each neuron (**Figure 1.4B**). Mean relative plaque load was decreased by 9% at 0-10 μm , but increased by 7% at 11-20 μm , 4% at

21-50 μm , and 10% at 51-100 μm . Median relative plaque load was decreased at all distances except 51-100 μm when compared to overall plaque load of the entire field of view. Paired sample t-tests demonstrated significance of difference in relative plaque load at 0-10 μm and 21-50 μm but not at 11-20 μm when compared to 51-100 μm . Probability of finding a plaque and relative intensity of plaque staining were low at the neuron's center and higher near and around the neuron (**Figures 1.4C** and **1.4D**). Intensity of plaque staining was much higher near NeuN-positive neurons (**Figure 1.4D**) than near SST neurons (**Figure 1.3D**).

After imaging and analyzing plaques and NeuN-positive neurons, we imaged and analyzed extracellular A β and PV neurons in 5XFAD mice. Once again, we analyzed extracellular A β and PV neurons in separate channels before merging them into composite images (**Figure 1.5A**). We then used these composite images to generate boxplots of relative A β load as a function of distance from the boundary of the neuron (**Figure 1.5B**). Mean relative A β load was increased by 42% at 0-10 μm , 50% at 11-20 μm , and 12% at 21-50 μm , but decreased by 5% at 51-100 μm . Paired sample t-tests indicated significant difference in mean A β load at 0-10 μm and 11-20 μm but not 21-50 μm when compared to A β load at 51-100 μm . Probability of finding A β and relative intensity of A β staining were low at the neuron's center and higher in the PV neuron's local environment (**Figures 1.5C** and **1.5D**).

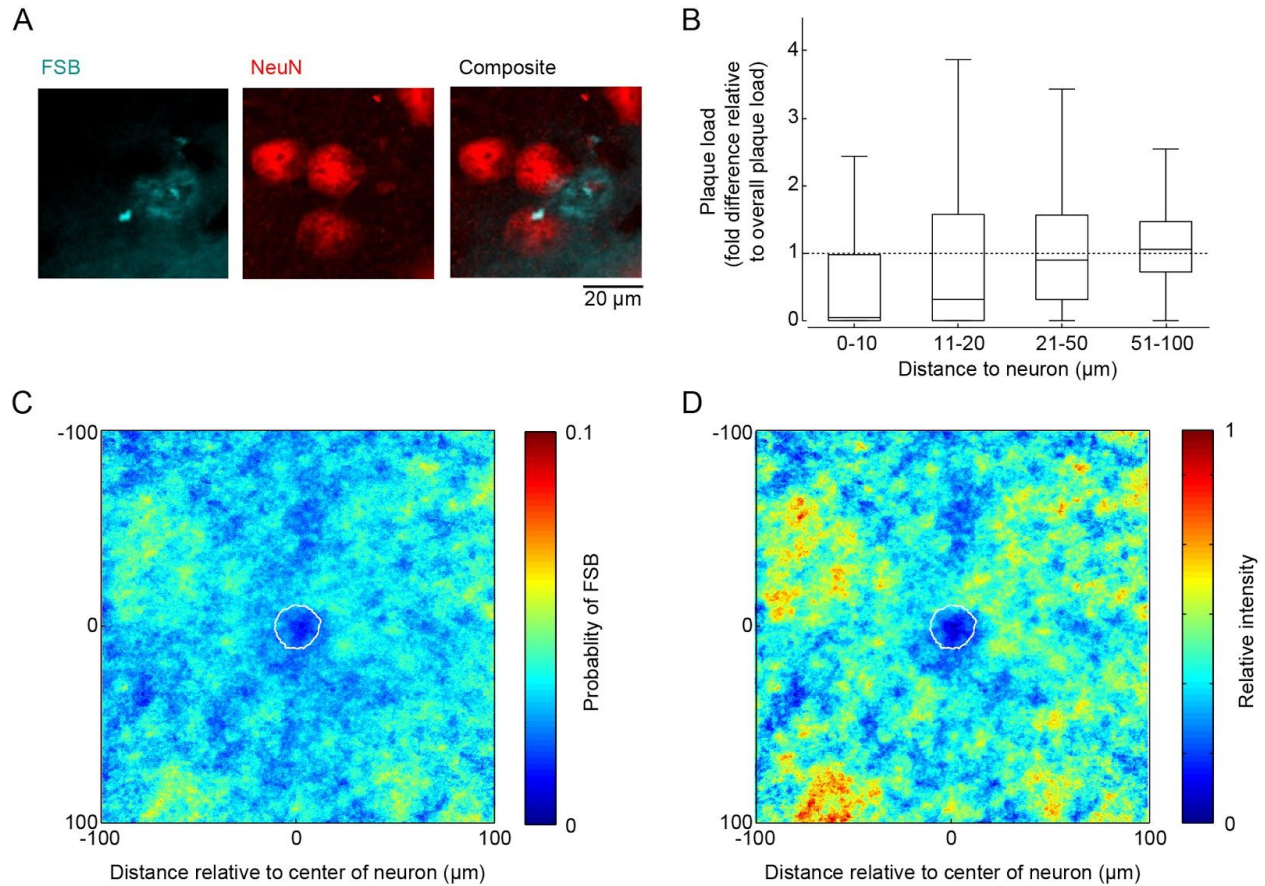


Figure 1.4. Plaques and NeuN-positive neurons in 5xFAD mice

(A) Example FSB staining of plaques (left), NeuN-positive neuron (middle) and composite (right).

(B) Same as Figure 2B but for NeuN-positive neurons. Relative plaque load (mean \pm SEM): 0.91 ± 0.05 , 0-10 μm ; 1.07 ± 0.04 , 11-20 μm ; 1.04 ± 0.03 , 21-50 μm ; 1.10 ± 0.01 , 51-100 μm . Paired sample t-tests indicated a significant difference between relative plaque load at 0-10 μm ($p = 1 \times 10^{-4}$) μm and 21-50 μm ($p = 0.05$) but not 11-20 μm ($p = 0.43$) compared to 51-100 μm . $n = 1440$ neurons, 5 animals.

(C) Same as Figure 1.2C but for NeuN-positive neurons.

(D) Same as Figure 1.2D but for NeuN-positive neurons.

Imaging and analysis of extracellular A β and PV neurons in 5XFAD mice were followed by imaging and analysis of intracellular A β and PV neurons in 5XFAD mice. We analyzed intracellular A β and PV neurons in separate channels before merging those channels to produce composite images (**Figure 1.6A**). Composite

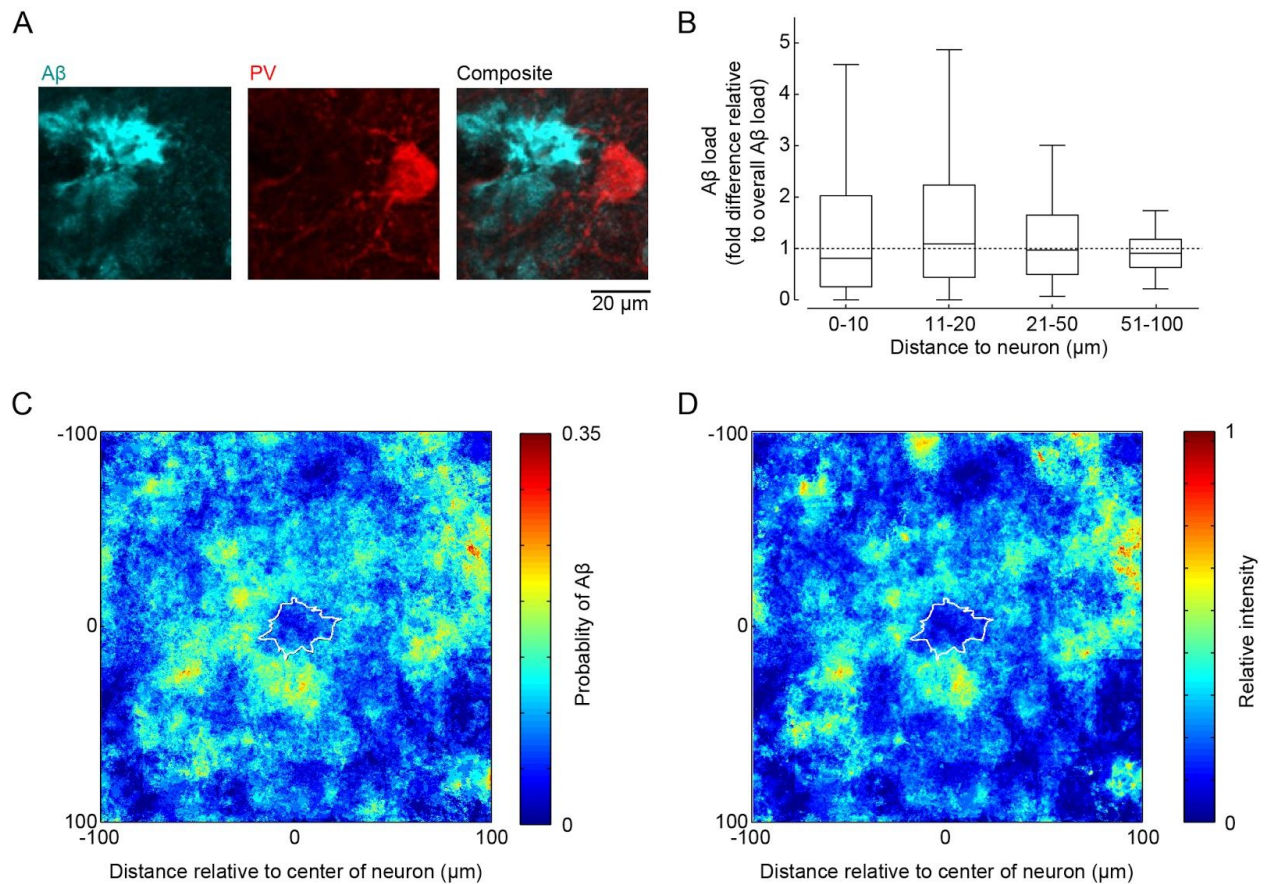


Figure 1.5. Extracellular Aβ and PV neurons in 5XFAD mice.

(A) Example staining of extracellular amyloid-β (left), SST neuron (middle) and composite (right).

(B) Same as Figure 2B but for extracellular Aβ and PV neurons. Relative plaque load: 1.42 ± 0.19 , 0-10 μm; 1.50 ± 0.16 , 11-20 μm; 1.12 ± 0.09 , 21-50 μm; 0.95 ± 0.05 , 51-100 μm. Paired sample t-tests indicated a significant difference between relative Aβ load at 0-10 μm ($p = 0.04$) and 11-20 μm ($p = 0.004$) but not 21-50 μm ($p = 0.18$) compared to 51-100 μm. $n = 73$ neurons, 5 animals.

(C) and (D) Same as Figure 1.2C and 1.2D but for extracellular Aβ and PV neuron.

images were used to create boxplots of relative intracellular Aβ load as a function of distance to the boundary of the PV neuron (**Figure 1.6B**). Mean relative Aβ load was decreased by 11% at 0-10 μm, increased by 9% at 11-20 μm, increased by 18% at

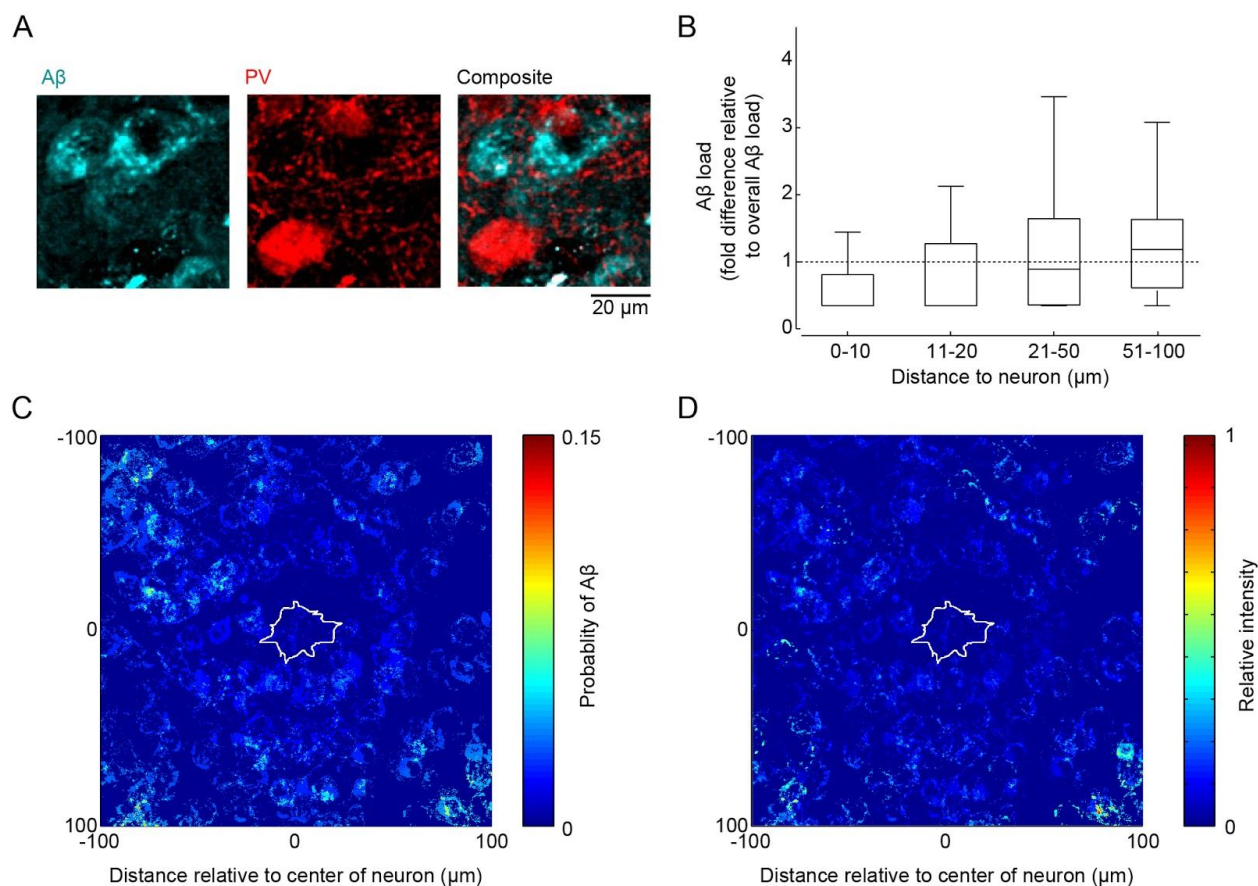


Figure 1.6. Intracellular A β and PV neurons in 5XFAD mice.

(A) Example staining of extracellular amyloid- β (left), PV neuron (middle) and composite (right).

(B) Same as Figure 2B but for intracellular A β and PV neurons. Relative A β load (mean \pm SEM): 0.89 \pm 0.27, 0-10 μ m; 1.09 \pm 0.28, 11-20 μ m; 1.18 \pm 0.19, 21 - 50 μ m; 0.90 \pm 0.07, 51-100 μ m. Paired sample t-tests indicated no significant difference between relative A β load at 0-10 μ m ($p = 0.94$) μ m, 11-20 μ m ($p = 0.56$), and 21-50 μ m ($p = 0.22$) compared to 51-100 μ m. $n = 73$ neurons, 5 animals.

(C) and (D) Same as Figure 1.2C and 1.2D but for intracellular A β and PV neuron.

21-50 μ m, and decreased by 10% at 51-100 μ m. Paired sample t-tests demonstrated no significance in difference of relative A β load at any distance when compared to relative A β load 51-100 μ m. Probability of finding intracellular A β and relative intensity of

intracellular A β staining were low both at the PV neuron's center and in the PV neuron's local environment (**Figures 1.6C** and **1.6D**).

Lastly, after imaging and analyzing intracellular A β and PV neurons in 5XFAD mice, we imaged and analyzed A β and PV neurons in postmortem brain tissues of AD patients. A β and PV neurons were analyzed in separate channels before being merged into composite images (**Figure 1.7A**). We then used these composite images to create boxplots of relative A β load as a function of the distance to the boundary of the PV neuron (**Figure 1.7B**). Mean relative A β load increased by 64% at 0-10 μ m, 73% at 11-20 μ m, and 18% at 21-50 μ m, but decreased by 5% at 51-100 μ m. Paired sample t-tests indicated significance in difference in relative A β load at all distances when compared to relative A β load at 51-100 μ m. Here, probability of finding A β and relative intensity of A β staining were slightly lower at the PV neuron's center, higher in the region immediately surrounding the PV neuron, and lower at distances far from the PV neuron's center (**Figure 1.7C** and **1.7D**).

Discussion

We used immunohistochemical methods to investigate the relationship between PV neurons and A β plaques in the Cg1/M2 cortical regions of brain tissue obtained from 5XFAD mice and human postmortem brain tissue obtained from AD patients. We also analyzed composite imaging of plaques and SST neurons and of plaques and NeuN-positive neurons. We found that the local environment of PV neurons in the Cg1/M2 of mice and human brain tissues demonstrated an increased vulnerability to the

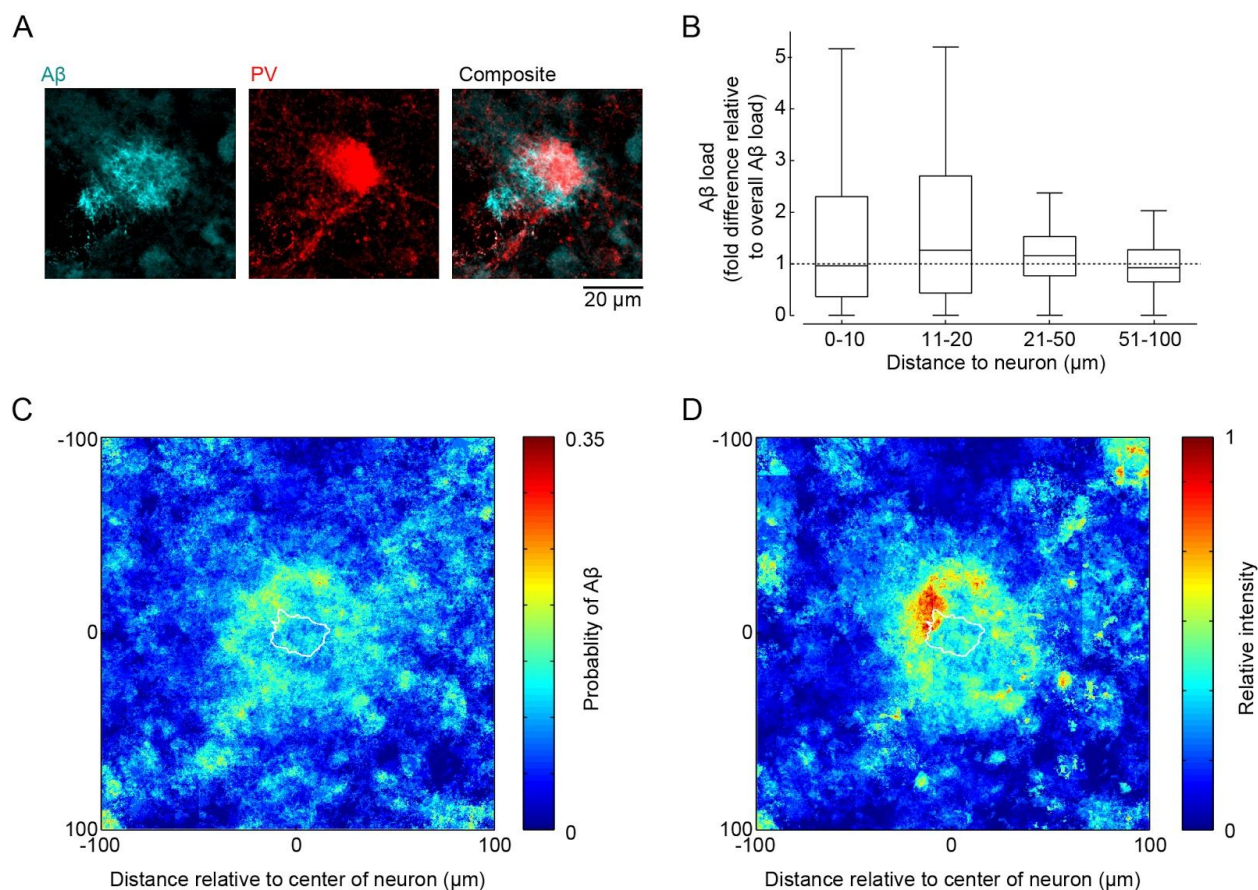


Figure 1.7. A β and PV neurons in post-mortem human brain tissues of AD patients. (A) Example staining of amyloid- β (left), PV neuron (middle) and composite (right). (B) Same as Figure 2B but for A β and PV neurons in human brain tissues. Relative A β load (mean \pm SEM): 1.64 ± 0.22 , 0-10 μm ; 1.73 ± 0.20 , 11-20 μm ; 1.18 ± 0.08 , 21-50 μm ; 0.95 ± 0.05 , 51-100 μm . Paired sample t-tests indicated significant difference between relative A β load at 0-10 μm ($p = 0.007$), 11-20 μm ($p = 0.001$) and 21-50 μm ($p = 0.03$) compared to 51-100 μm . $n = 68$ neurons, 4 AD patients. (C) and (D) Same as Figure 1.2C and 1.2D but for A β and PV neurons in human brain tissues.

accumulation of nearby A β and plaques. Meanwhile, we observed a decrease in mean relative plaque load in regions closest to SST neurons in 5XFAD mice tissue. In the following discussion, I will interpret the results of the imaging and analysis of A β plaques and each neuron type in further detail. I will lastly address the significance of these

findings in light of the broader mission to investigate the relationship between A β plaque pathology and PV interneurons, as well as what questions remain that should be of interest in future study.

We found that mean relative plaque load, probability of finding plaques, and intensity of plaque staining were increased near and around PV neurons when compared to overall fields of view in the brain tissues of 5XFAD mice. Mean relative plaque load was increased by 30% and 43% at distances of 0-10 μ m and 11-20 μ m to the neuron's boundary, both of which were statistically significant in difference when compared to mean relative plaque load at far distances, or 51-100 μ m (**Figure 1.2B**). The probability of finding a plaque and relative intensity of plaque staining were low at the neuron's center, but high near and around the neuron (**Figures 1.2C** and **1.2D**). These results suggest that, while the PV neuron is resistant to plaque formation, the microenvironment immediately surrounding the PV neuron is significantly more vulnerable to high plaque load than the overall field of view. Furthermore, these findings are consistent with the idea that PV interneurons may exhibit some sort of resistance to AD neuropathology. The idea that PV neurons may create a microenvironment that is conducive to plaque growth, however, is novel and worth further study.

While PV neurons demonstrated increased regional vulnerability to plaque accumulation, SST neurons demonstrated decreased regional vulnerability to plaques in mice brain tissues. Near SST neurons, mean relative plaque load was decreased by 32% at 0-10 μ m from the neuron boundary, which was statistically significant in difference when compared to mean relative plaque load at far distances (**Figure 1.3B**).

The probability of finding a plaque and relative intensity of plaque staining were much lower near and around SST neurons (**Figures 1.3C and 1.3D**) than around PV neurons (**Figures 1.2C and 1.2D**). Thus, while the microenvironment surrounding PV neurons was prone to increased plaque burden, the microenvironment immediately surrounding SST neurons was prone to decreased plaque burden.

After investigating the relationship between plaques and PV and SST interneurons, we analyzed plaque distribution patterns in relation to all neurons, as indicated by NeuN-positive staining in 5XFAD mice tissues. Plaques found near and around NeuN-positive cells were more numerous than those found near SST interneurons, but less numerous than those found near PV interneurons in tissues obtained from 5XFAD mice. Mean relative plaque load near NeuN-positive cells did not change by more than 10% when compared to overall plaque load of the whole field of view (**Figure 1.4B**). The probability of finding a plaque and relative intensity of plaque staining were low at the neuron's center, but moderate to high near and around the neuron (**Figure 1.4C and 1.4D**), and much higher than near SST neurons (**Figure 1.3D**). Thus, plaque burden near NeuN-positive neurons, an indicator for the general neuron population, was higher than the burden surrounding SST neurons, but lower than the burden surrounding PV neurons. These findings complement the preceding observation that plaque load near PV cells is higher than plaque load overall and that plaque load near SST cells is lower than plaque load overall.

Following analysis of plaque load near and around PV, SST, and NeuN-positive neurons, we analyzed A β load near and around PV cells in brain tissues from 5XFAD

mice. Near PV cells, mean relative extracellular A β load was increased by 42% at 0-10 μ m and by 50% at 11-20 μ m, both of which were significant in difference when compared to extracellular A β load at far distances (**Figure 1.5B**). As in the case of plaques located near PV cells, the probability of finding extracellular A β and relative intensity of extracellular A β staining were low at the neuron's center, but high near and around the PV cell (**Figures 1.5C** and **1.5D**). These results indicate that, like plaque load, extracellular A β load is substantially lower at the cell's center and higher in the microenvironment surrounding PV cells than in the general field of view in 5XFAD mice.

While extracellular A β load was very high near PV cells, however, intracellular A β load was very low near and around PV cells in mice brain tissues. Paired sample t-tests indicated no significant difference in mean relative intracellular A β load at any close distances when compared to mean relative intracellular A β load at far distances (**Figure 1.6B**), but the probability of finding intracellular A β and relative intensity of intracellular A β staining were generally low at all distances within 100 μ m from the neuron's center (**Figures 1.6C** and **1.6D**), and definitely much lower than probability and intensity of extracellular A β staining near PV neurons (**Figures 1.5C** and **1.5D**). So, while extracellular A β load is higher than average at distances close to PV cells, intracellular A β load is generally low near and around PV neurons in 5XFAD brain tissues, although any patterns in change in intracellular A β load as a function of distance from the PV neuron boundary are not presently clear or significant.

Lastly, just as in the case of plaques and extracellular A β near PV neurons in brain tissues from 5XFAD mice, mean relative A β load, probability of finding A β , and

intensity of A β staining were increased near and around PV neurons when compared to overall fields of view in the postmortem brain tissues of human AD patients. In postmortem tissues from human AD patients, mean relative A β load increased by 64% at 0-10 μ m and by 73% at 11-20 μ m from the PV neuron's boundary, both of which were significant in difference when compared to mean relative A β load at far distances (**Figure 1.7B**). As in the case of plaques and extracellular A β in mice tissue, probability of finding A β and relative intensity of A β staining in human tissue were very high immediately surrounding PV neurons (**Figures 1.7C and 1.7D**). Unlike in mice tissues, however, probability of finding A β and relative intensity of A β staining in human tissue were moderate to high at the PV neuron's center, and the contrast between intensity of A β staining at close distances and intensity at far distances was far more pronounced. Taken together, these findings indicate that the local vulnerability to plaque and extracellular A β load in the microenvironment immediately surrounding PV neurons in mice tissue is consistent with regional vulnerability to A β load surrounding PV neurons in human tissue.

Hence, in the present study, we have demonstrated that local areas near and around PV neurons in the Cg1/M2 cortical regions of brain tissues from 5XFAD mice and human AD patients are characterized by elevated vulnerability to high plaque and A β load, while SST neurons in the same cortical region of tissues from 5XFAD mice are characterized by diminished regional vulnerability to plaques. These findings contribute significantly to efforts to characterize the interactions between interneurons, A β , and

plaques observed in AD pathology while also presenting several opportunities for further inquiry.

One such area of interest is why the PV neuron microenvironment is more conducive to A β and plaque aggregation, while the SST neuron microenvironment is less conducive to A β and plaque aggregation when compared to the general neuronal population in 5XFAD mice. It is possible that these findings may be related to differences in neural activity between PV cells, SST cells, and the general neuronal population. In a study of extracellular A β deposition in 5XFAD mice, Yuan and Grutzendler used viral-mediated delivery of designer receptors exclusively activated by designer drugs (DREADDs) to modulate neural activity in regions containing DREADD-expressing neurons, observing that when they increased neural activity, regional A β deposition was increased, and when they decreased neural activity, regional A β deposition was decreased (2016). In other words, areas of higher neural activity were correlated with greater A β deposition. PV cells are known to display high rates of neural activity, while SST cells fire less frequently (Vargova, Vogels, Kostecka, & Hromadka, 2018). It is then possible that areas near and around PV cells may be characterized by greater extracellular A β load due to the high neural activity of PV cells, and areas near SST cells may be characterized by lower extracellular A β load due to relatively lower neural activity. Thus far, however, this hypothesis has not been thoroughly tested.

Other opportunities for further inquiry include efforts to understand why plaque and A β burden is low on average at the PV neuron's center in 5XFAD and human

tissues, whether or not observed plaque aggregation is correlated with PV interneuron death, and how vulnerability to death is correlated with plaque distribution in relation to PV interneuron type; the latter two questions will be the subject of investigation in Chapter Two.

Chapter Two: Examining PV Neuron Subtypes in the 5XFAD Mouse Model

Introduction

In the previous chapter, it was demonstrated that the microenvironment surrounding PV interneurons is particularly conducive to extracellular accumulation of A β and amyloid plaques in the cortices of 5XFAD mouse models. It is known that, in 5XFAD mice, intraneuronal A β 42 accumulation, amyloid deposition, and the formation of extracellular neurotoxic amyloid plaques are followed by local neural death by apoptosis (Eimer & Vassar, 2013). Neurons die for a variety of reasons regardless of proximity to plaques; however, of particular interest here is whether or not the A β and plaques found near PV interneurons in 5XFAD mice are correlated with PV cell death.

Researchers in the Kwan Laboratory have found that plaques are indeed correlated with PV cell death in 5XFAD mice tissues (Ali, n.d.). In 5XFAD mice, more large plaques are observed in the deep cortical layers than in the superficial cortical layers, with the largest plaque burden existing in the cingulate and secondary motor cortex (Ali, n.d.). Correspondingly, while PV neural density is unaltered in the superficial cortical layers of 5XFAD mice, PV neuron density is decreased in the deep cortical layers by up to 50% in the cingulate and by 39% in the secondary motor cortex (Ali, n.d.). In other words, the deep layers of the frontal cortex are particularly vulnerable to large plaque burden as well as decreased PV density in 5XFAD mice tissues (Ali, n.d.).

Therefore, it is understood not only that PV interneurons are found near larger amyloid plaques than non-PV neurons, but also that plaques are correlated with PV cell death in 5XFAD mice; what remains unknown, however, is how the relationship

between plaques and PV cells differs by PV cell subtype. PV interneurons can be categorized as either basket cells or chandelier cells. Basket cells are inhibitory GABAergic interneurons that innervate the soma of excitatory cells by forming basket-like structures around the innervated cell bodies. Chandelier cells, on the other hand, are inhibitory GABAergic interneurons that innervate the axon initial segment (AIS) of pyramidal excitatory neurons in order to regulate the initiation of action potentials (Taniguchi, Lu, & Huang, 2013). The effect of PV cell subtype on the previously observed patterns of A β and plaque load surrounding PV cells, plaque size, and PV cell death are thus far unknown.

The purpose of the present research is to investigate, using immunohistochemical staining how neuron density in 5XFAD mice differs in two subtypes of PV cells: basket cells and chandelier cells. Both PV subtypes and their targets will be identified and visualized by fluorescently labeling the cell bodies targeted by basket cells and the axon initial segments targeted by chandelier cells. The results of this study will yield a more nuanced understanding of the role of PV interneuron subtype in patterns of PV cell loss observed in FAD neuropathology.

Materials and Methods

Animals

As described in Chapter One, 5XFAD mice were obtained from Jackson Laboratory (Stock No. 006554, also called MMRRC Stock No. 34840-JAX). Male 5XFAD mice were mated with female WT mice (C57BL/6J WT strain from Jackson Laboratory, Stock No.

000664) to produce 5XFAD and WT littermates. From these litters, male 5XFAD mice and male wild type (WT) littermate controls aged 6-9 months were obtained, and genotypes were confirmed by polymerase chain reaction. Procedures were approved by the Yale University Institutional Animal Care and Use Committee.

Immunohistochemistry

Mice were sacrificed and perfused transcardially according to the procedure described in the *Immunohistochemistry* section of Chapter One. Slices were then subjected to free-floating staining as follows.

Ankyrin-G and PV staining on mouse tissue. Mouse tissues were stained for ankyrin-G and PV according to the methods outlined in the section of Chapter One titled, *Immunohistochemistry: A β and PV staining on mouse and human tissue*, with the following exceptions. Instead of polyclonal mouse anti-A β antibody, slices were stained with anti-ankyrin-G antibody (Millipore Sigma MABN466 clone N106/36; 1:250 final dilution), and slices were not incubated in formic acid. 10 slices were stained from 5 WT mice, and 10 slices were stained from 5 5XFAD mice.

Neuronal nuclei (NeuN) and PV staining on mouse tissue. Three methods for NeuN and PV staining were tested. In the first method, conjugated anti-NeuN antibody was tested on 5XFAD mouse tissue slices in order to assess the possibility of conducting parallel NeuN and PV staining using conjugated primary antibodies as follows. Slices from mouse tissue were incubated for 1 hour in blocking solution (0.5% Triton and 5% goat serum in PBS) at room temperature. Slices were incubated overnight for at least 12

hours in conjugated anti-NeuN antibody (rabbit monoclonal to NeuN, Alexa Fluor 488, Abcam ab190195; 1:200 final dilution) at 4°C. Slices were washed in PBS three times and then incubated for 10 minutes in distilled water at room temperature before mounting onto slides. Slides were dried in the dark for at least two hours at room temperature or overnight at 4°C. After drying, slides were coverslipped with DPX mounting medium (06522, MilliporeSigma). Coverslipped slides were dried and stored for long term usage in slide boxes at 4°C. Bovine serum albumin (BSA) removal and conjugation of primary polyclonal rabbit anti-PV antibody (Abcam ab11427, 1:1000 dilution in blocking solution) were also tested, using the Abcam BSA removal kit (ab173231) and the Alexa Fluor™ 546 Antibody Labeling Kit (#A20183). Slices were stained with BSA-removed, conjugated anti-PV antibody according to the procedure outlined above for conjugated anti-NeuN antibody staining. In the second method, slices were stained sequentially first for PV and then for NeuN as follows. Slices from mouse tissue were incubated for 1 hour in blocking solution (0.5% Triton and 5% goat serum in PBS) at room temperature. Slices were incubated overnight for at least 12 hours in primary polyclonal rabbit anti-PV antibody (Abcam ab11427, 1:1000 dilution in blocking solution) at 4°C. Slices were washed three times in PBS and then incubated for 2 hours in secondary antibody (goat anti-rabbit IgG H&L Alexa Fluor 555, Abcam ab150078, 1:500 dilution in blocking solution) at room temperature. Slices were washed three times in PBS once more before incubating overnight again for at least 12 hours in primary monoclonal rabbit anti-NeuN antibody (Abcam ab177487, 1:500 dilution) at 4°C. Slices were washed three times in PBS and then incubated for 3 hours in secondary antibody

(goat anti-rabbit IgG H&L Alexa Fluor 488, Abcam ab150077, 1:500 dilution in blocking solution) at room temperature. Lastly, slices were washed again in PBS three times and then incubated for 10 minutes in distilled water at room temperature before mounting onto slides. Slides were dried in the dark for at least two hours at room temperature or overnight at 4°C. After drying, slides were coverslipped with DPX mounting medium (06522, MilliporeSigma). Coverslipped slides were dried and stored for long term usage in slide boxes at 4°C. In the third method, slices were stained for PV and NeuN according to the methods outlined in the section of Chapter One titled, *Immunohistochemistry: A β and PV staining on mouse and human tissue*, with the following exceptions. Instead of polyclonal mouse anti-A β antibody, slices were stained with mouse anti-NeuN antibody (Millipore Sigma MAB377 clone A60; 1:200 final dilution), and slices were not incubated in formic acid.

Imaging

We used a widefield fluorescence microscope (Olympus BX61) and its accompanying software for all imaging. We identified the frontal regions (Cingulate 1, Cg1, and secondary motor area, M2) to be imaged using landmarks such as white matter and ventricles. After delineating the area to be imaged, the filter for NeuN or Ankyrin-G (460-510 nm) was used for imaging. We took nonoverlapping images (512 x 419 pixels/image) at random locations in Cg1 and M2 using a 10x objective. Images were then pseudocolored in the image processing software, Fiji.

Results

We stained slices for PV and ankyrin-G in parallel, for PV and NeuN sequentially and in parallel, and for NeuN using a conjugated primary antibody. To assess the efficacy of each staining protocol, we took sample images of ankyrin-G and NeuN-positive neuronal staining in the Cg1/M2 cortical regions of brain tissue obtained from 5XFAD mice.

First, in order to determine the probability of PV labeling given labeled ankyrin-G, 5XFAD cortical tissues were stained in parallel for PV and ankyrin-G. Anti-ankyrin-G staining did fluorescently label some axon initial segments, but overall, staining was dim and not very distinct in comparison to background fluorescence (see an example image in **Figure 2.1**). Within this example image, axon initial segments can be visualized, in addition to the outlines of PV cells labeled with fluorophore attached-secondary antibody (555 nm) bleeding through the 460-510 nm filter used to capture this image. This image was captured using a widefield fluorescence microscope with 800 ms exposure time and colored blue by image processing in Fiji to replicate the blue light emitted by the fluorophore attached to the secondary antibody (495 nm). So, ankyrin-G staining via the PV and ankyrin-G parallel staining protocol was present, but dim.

Next, to determine the probability of PV labeling given labeled NeuN, 5XFAD cortical tissues were stained using conjugated anti-NeuN antibody only in order to test the possibility of using conjugated anti-NeuN and conjugated anti-PV antibodies simultaneously for parallel PV and NeuN staining (**Figure 2.2**). Within this image, NeuN labeling cannot be identified. This image was captured using a widefield fluorescence

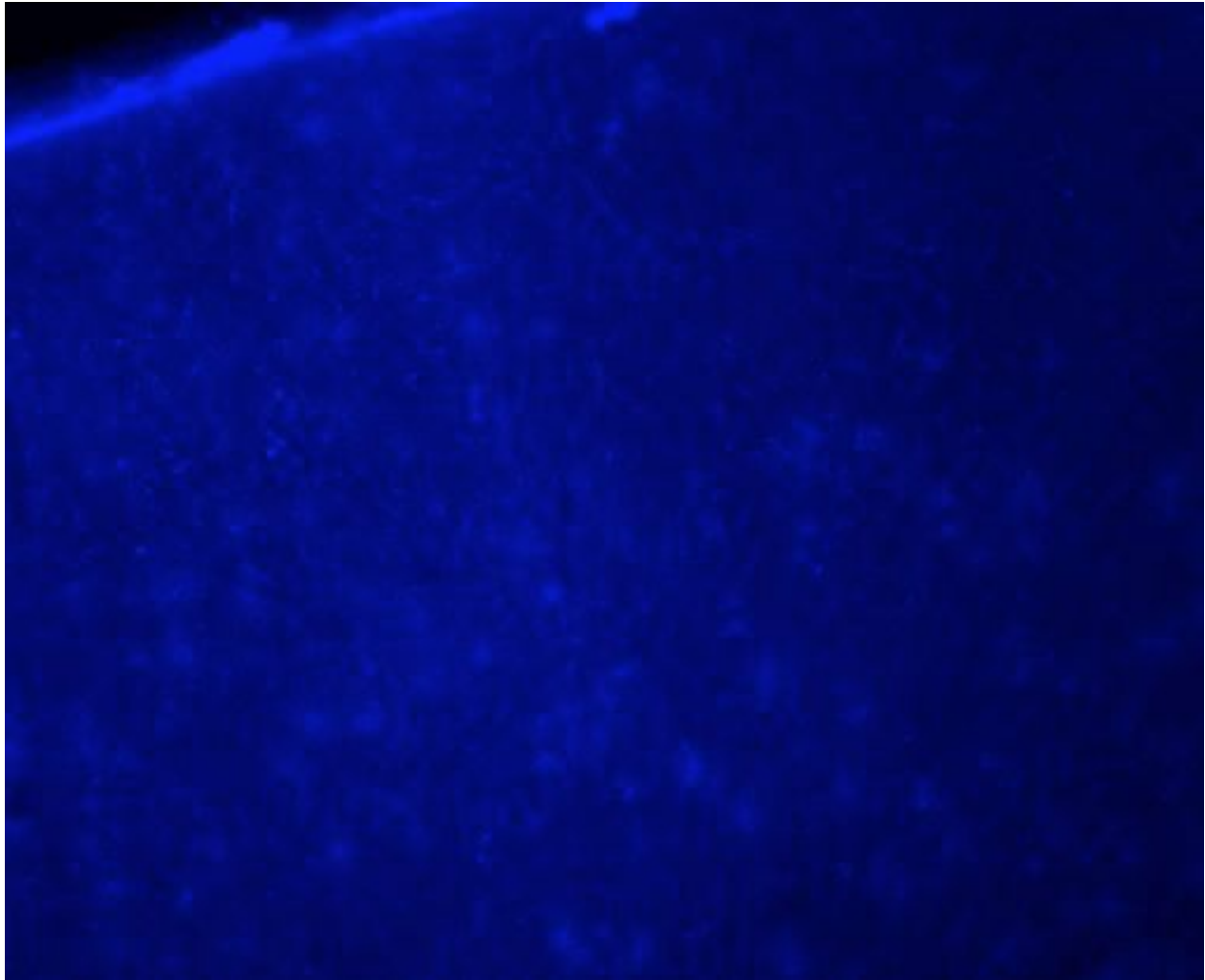


Figure 2.1. Ankyrin-G after parallel Ankyrin-G and PV staining in 5XFAD mice. Example of ankyrin-G staining on 5XFAD brain tissue imaged on a widefield fluorescence microscope using a 460-510 nm filter (512 x 419 pixels/image). Image was captured in black and white and pseudocolored in Fiji.

microscope with 200 ms exposure time and colored blue by image processing in Fiji in order to replicate the blue light emitted by the fluorophore-conjugated antibody (488 nm). So, staining with conjugated anti-NeuN antibody was unsuccessful.

Given that conjugated NeuN antibody staining was unsuccessful in 5XFAD tissues, PV and NeuN labeling in 5XFAD tissues was attempted via a sequential

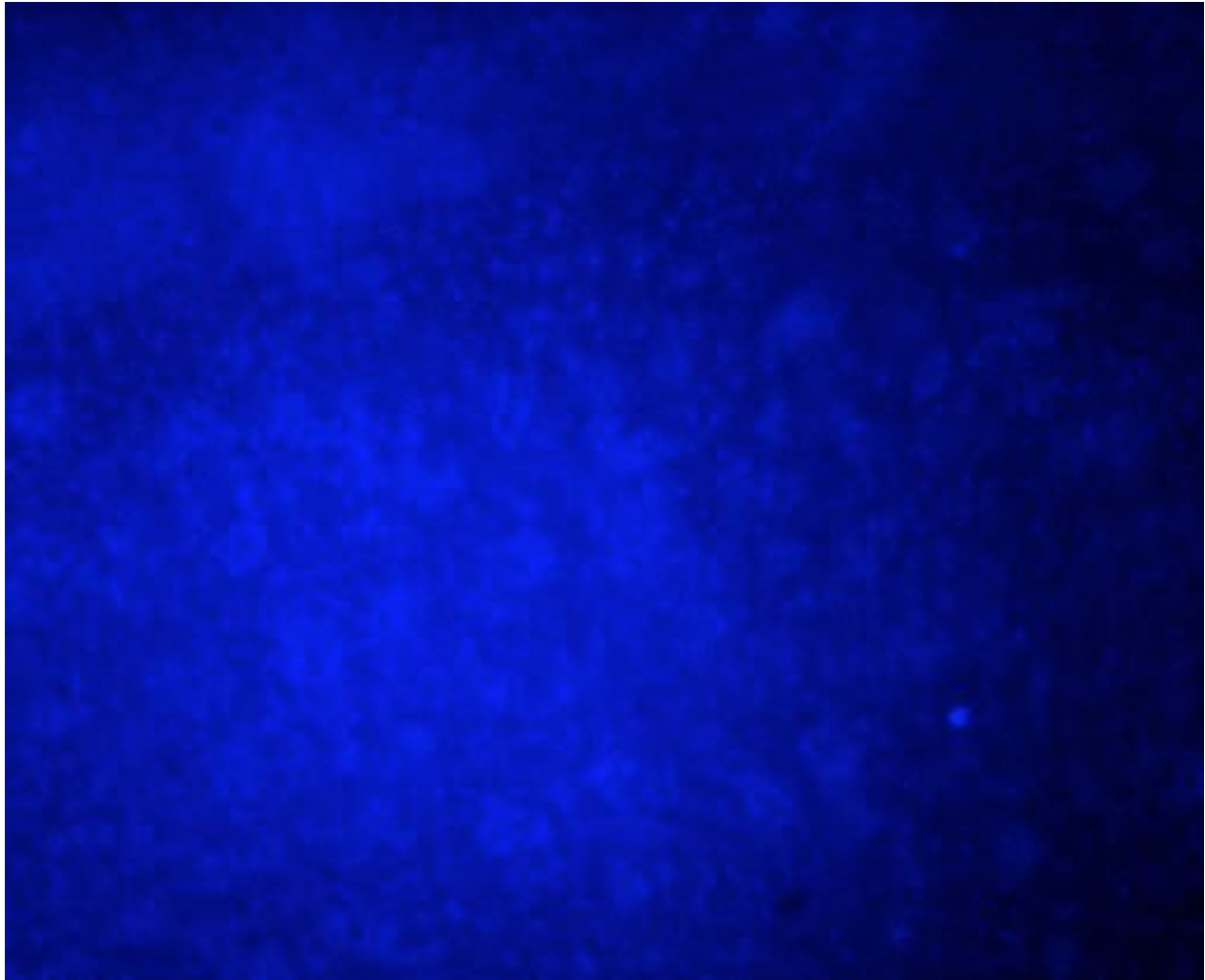


Figure 2.2. Conjugated NeuN in 5XFAD mice.

Example of conjugated NeuN staining on 5XFAD brain tissue imaged on a widefield fluorescence microscope using a 460-510 nm filter (512 x 419 pixels/image). Image was captured in black and white and pseudocolored in Fiji.

staining protocol. Here, NeuN staining was absent, and the neurons labeled were PV neurons, indicating that the secondary antibody against primary anti-NeuN antibody fluorescently labeled primary anti-PV antibody instead (**Figure 2.3**). This image was captured using a widefield fluorescence microscope with 500 ms exposure time and colored blue by image processing in Fiji to replicate the blue light emitted by the

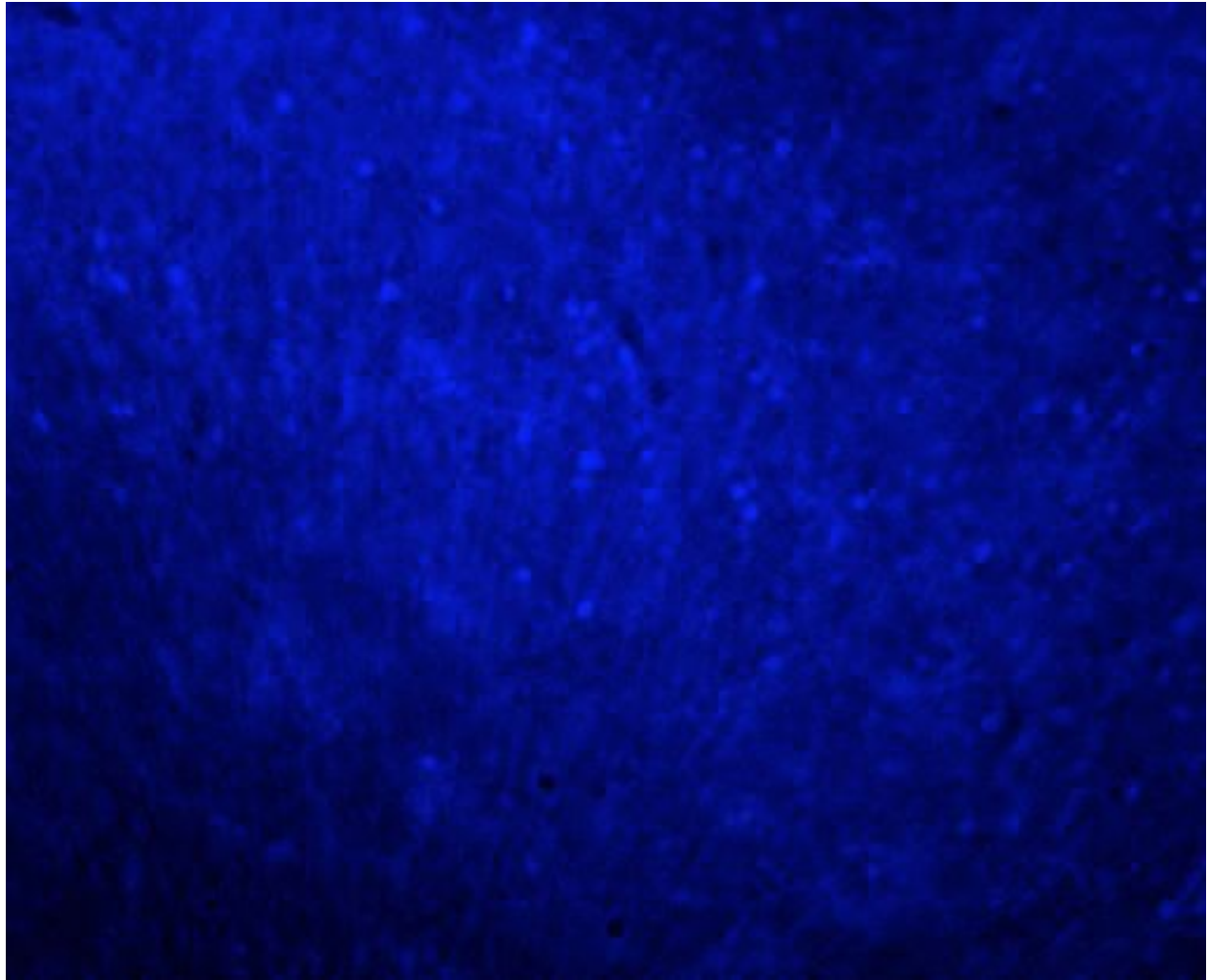


Figure 2.3. NeuN after sequential PV and NeuN staining in 5XFAD mice.

Example of NeuN staining after sequential PV and NeuN staining on 5XFAD brain tissue imaged on a widefield fluorescence microscope using a 460-510 nm filter (512 x 419 pixels/image). Image was captured in black and white and pseudocolored in Fiji.

fluorophore-conjugated antibody (488 nm). So, staining for NeuN via the sequential PV and NeuN protocol was also unsuccessful.

After the unsuccessful conjugating NeuN staining and sequential PV and NeuN staining in 5XFAD tissues, PV and NeuN labeling in 5XFAD tissues was attempted via a parallel staining protocol. Imaging of NeuN staining revealed that NeuN-positive

neurons were successfully labeled, though dim (**Figure 2.4A**). Images also indicated that the secondary goat anti-mouse antibody (Abcam ab150117, Alexa Fluor 495) stained not only mouse anti-NeuN antibody, but also antigens present in the blood vessels in the mouse tissues (**Figure 2.4B**). Both images were captured using a widefield fluorescence microscope with 500 ms exposure time and colored blue by image processing in Fiji to replicate the blue light emitted by the fluorophore-conjugated antibody (495 nm). So, parallel PV and NeuN staining resulted in dim and nonspecific NeuN labeling.

Discussion

We used immunohistochemical methods in efforts to fluorescently label PV cell subtypes and their targets in order to investigate how loss of PV neuron density observed in 5XFAD mice tissues differs by PV cell subtype. In order to visualize chandelier cells and targeted axon initial segments, we stained 5XFAD cortical slices via parallel anti-PV and anti-ankyrin-G staining. In order to visualize basket cells and their cell body targets, we attempted to stain slices for PV and NeuN using three methods, including use of a conjugated anti-NeuN antibody, sequential PV and NeuN staining, and parallel PV and NeuN staining. While attempts to stain NeuN-positive neurons via the conjugated anti-NeuN antibody and sequential PV and NeuN staining were ultimately unsuccessful, we found that anti-ankyrin-G labeling and NeuN-positive neuron labeling via the parallel PV and NeuN protocol were partially successful. In the following discussion, I will interpret the results of the example images and address

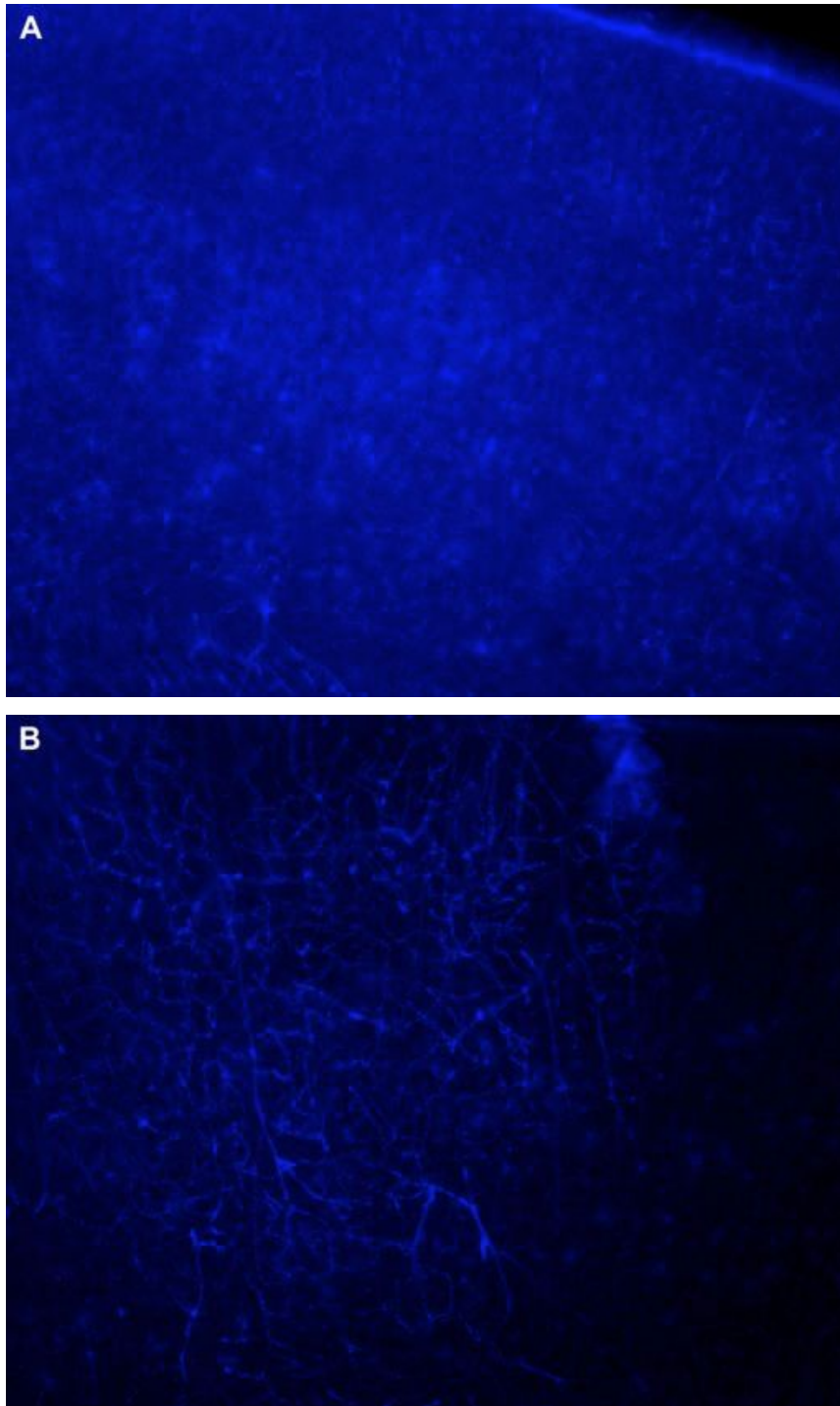


Figure 2.4. NeuN after parallel PV and NeuN staining in 5XFAD mice.

(A) Example of NeuN staining after parallel PV and NeuN staining on 5XFAD brain tissue imaged on a widefield fluorescence microscope using a 460-510 nm filter (512 x 419 pixels/image). Image was captured in black and white and pseudocolored in Fiji.

(B) Example of blood vessel staining after parallel PV and NeuN staining on 5XFAD brain tissue imaged under the same conditions as (A).

potential reasons underlying the failed staining attempts in efforts to suggest what steps may be taken moving forward so that we may continue to work towards achieving the aforementioned goals of the study. The results of such future experiments will ultimately afford a better understanding of the role of PV interneuron subtype in patterns of PV cell loss observed in FAD neuropathology.

Widefield images of ankyrin-G labeling following parallel staining of 5XFAD cortical tissues for ankyrin-G and PV-positive interneurons revealed that axon initial segments were successfully labeled, although staining was dim and not very distinct when compared to background fluorescence and the fluorescence leaking into the ankyrin-G channel from the PV channel (**Figure 2.1**). In this example image, the PV cells can be visualized slightly while in the ankyrin-G channel because the fluorophores conjugated with the secondary antibodies used in this parallel staining procedure only differ in emitted wavelength by 60 nm. Ankyrin-G, which is labeled with a secondary antibody that is attached to Alexa Fluor 495 nm, is visualized by use of the 460-510 nm filter, but the PV cells, which are labeled with a secondary antibody that is attached to Alexa Fluor 555, emit a wavelength that is only 45 nm outside of the filter's target range. As a result, the fluorophores attached to the PV cells are slightly excited while visualizing the fluorescently labeled ankyrin-G, making the PV cells faintly visible. Overall, this image was quite dim, but axon initial segments are indeed visibly labeled, so this protocol for parallel ankyrin-G and PV staining should be used in future experiments in order to determine the probability of PV labeling given clearly labeled

ankyrin-G in 5XFAD cortical tissues. In doing so, we can quantify how much of PV cell density loss is attributed to loss of chandelier cells in 5XFAD.

Next, widefield images of NeuN-positive neuron labeling following staining with conjugated anti-NeuN antibody indicated that staining with conjugated anti-NeuN antibody was unsuccessful (**Figure 2.2**). In this example image, NeuN labeling is not present. It is possible that labeling with conjugated anti-NeuN antibody failed because not enough antibody was bound to NeuN. According to troubleshooting resources published by Abcam, this inability to bind can happen as a result of poor antibody solution homogenization; incubation for too short of a time period; making the concentration of the antibody too low; damage to the antibody (i.e. by prolonged exposure to light or changes in temperature); making the concentration of nuclei-permeabilizing agent, Triton, in the blocking solution too low; or not blocking for a long enough time period ("Troubleshooting and Using Controls," 2019). So, if we were interested in returning to efforts to stain NeuN-positive neurons with conjugated anti-NeuN antibody, then it would be wise to troubleshoot the staining protocol in light of these potential locations of error.

After our attempts to stain NeuN-positive neurons with conjugated anti-NeuN antibody failed, we next tried to stain for NeuN-positive neurons via a sequential PV and NeuN protocol, which also failed (**Figure 2.3**). In this case, NeuN staining was absent, and the secondary antibody against primary anti-NeuN antibody instead labeled primary anti-PV antibody. In order to reduce such nonspecific staining in any future attempts to stain for PV and NeuN-positive neurons sequentially, it may be helpful to reduce the

concentration of secondary antibody, increase the concentration of primary anti-NeuN antibody, or use a different primary anti-NeuN antibody.

Lastly, given that staining with conjugated anti-NeuN antibody and sequential PV and NeuN staining were unsuccessful, we tried staining 5XFAD tissues for PV and NeuN in parallel and using a different anti-NeuN antibody, resulting in successful labeling of NeuN-positive neurons, though dim and nonspecific (**Figure 2.4**). In addition to NeuN-positive neurons, antigens present in blood vessels were also labeled (**Figure 2.4B**). The antigens present in blood vessels were most likely labeled because the secondary goat anti-mouse antibody used in this protocol reacts with all mouse immunoglobulin G (IgG), as well as with light chains found within other mouse immunoglobulins ("Alexa Fluor® 488 Goat Anti-Mouse," 2019), and immunoglobulins such as IgG are abundant in the blood; so, if perfusion of the 5XFAD tissues and fixation in PFA left behind any residual blood, then antigens or immunoglobulins in the blood may have been bound by the secondary goat anti-mouse antibody. In order to reduce such nonspecific staining, Abcam recommends reducing the concentration of secondary antibody or using a primary antibody raised against an animal other than the species of the host tissue ("Troubleshooting and Using Controls," 2019). Furthermore, resolution of this staining could be improved by reducing the fluorescence of the background. Abcam reports that high background fluorescence can generally be decreased by increasing blocking incubation time, decreasing the primary antibody concentration, ensuring that secondary antibody is not binding nonspecifically, washing in PBS more extensively between staining, and using a secondary antibody fluorophore

that is less similar to the green range of autofluorescence often caused by PFA fixation ("Troubleshooting and Using Controls," 2019). Nonetheless, we successfully achieved the staining of NeuN-positive neurons using this protocol; so, this protocol for parallel NeuN and PV staining should be used in future experiments in order to determine the probability of PV labeling given clearly labeled NeuN-positive neurons in 5XFAD cortical tissues. In doing so, we can quantify how much of PV cell density loss is attributed to loss of basket cells in 5XFAD.

Moving forward, staining of chandelier and basket PV cells and their respective targets should be achieved by conducting parallel PV and ankyrin-G staining and parallel PV and NeuN staining on 5XFAD cortical tissues according to the methods outlined in this study. For parallel PV and NeuN staining, nonspecific staining of blood vessels can be addressed by reducing the concentration of secondary antibody or by using a primary antibody raised against an animal other than the mouse. For both protocols, background fluorescence can be reduced by ensuring routine and thorough PBS washes between each step, increasing blocking incubation time, and using a secondary antibody fluorophore that is less similar to the green range of autofluorescence often caused by PFA fixation. Lastly, in order to ensure optimal interaction between antigen and antibody, antibody solutions should be thoroughly homogenized, and an adequate concentration of nuclei-permeabilizing agent, Triton, should be present in the blocking solution. Taken together, these technical considerations should help to optimize the clarity and efficacy of parallel PV and NeuN and parallel PV and ankyrin-G staining, affording methods by which we can properly

investigate the role of PV interneuron subtype in patterns of PV cell loss observed in FAD neuropathology.

Conclusions and Future Study

The purpose of the present study was to address gaps in knowledge regarding the roles of interneurons in AD by examining patterns of A β and plaque distribution in relation to interneuron types in 5XFAD and human tissues as well as how PV interneuron density differs by cell subtype in 5XFAD.

We first investigated the relationship between PV neurons and A β and plaques in the Cg1/M2 cortical regions of 5XFAD mouse tissue and postmortem brain tissue from human AD patients. We also analyzed patterns of plaque distribution in relation to SST neurons and NeuN-positive neurons. We found that local areas near and around PV neurons in the Cg1/M2 cortical regions of brain tissues from 5XFAD mice and human AD patients were characterized by elevated vulnerability to high plaque and A β load, while SST neurons in the same cortical region of tissues from 5XFAD mice were characterized by lower local vulnerability to plaques compared to the general neuronal population. Interestingly, plaque and A β load were low at the center of PV neurons in both 5XFAD and human tissues. In other words, PV interneurons displayed low plaque and A β load in the cell, but were surrounded by a microenvironment that was particularly conducive to greater aggregation of plaques and extracellular A β than other neuronal areas for reasons that are unknown.

After analyzing the relationships between A β , plaques, PV, and SST in 5XFAD mouse and postmortem samples from human AD patients, we examined how neuron density differs in basket PV cells versus chandelier PV cells in 5XFAD mice, given the finding that proximity to plaques is correlated with loss of PV cell density (Ali, n.d.).

PV cell types and their targets were identified and visualized by fluorescently labeling the cell bodies targeted by basket cells with anti-NeuN antibody and the axon initial segments targeted by chandelier cells with anti-ankyrin-G antibody. While attempts to stain NeuN-positive neurons via the conjugated anti-NeuN antibody and sequential PV and NeuN staining were ultimately unsuccessful, we found that anti-ankyrin-G labeling and NeuN-positive neuron labeling via the parallel PV and NeuN protocol were fairly successful and worth pursuing for future study given the following technical adjustments. To reduce nonspecific staining, it is advisable that the concentration of secondary antibody be reduced or that we use a primary antibody raised against an animal other than the species of the host tissue. To reduce background fluorescence, we should ensure thorough PBS washes, increase blocking incubation time, and consider using a secondary antibody fluorophore that is less similar to the green range of autofluorescence often caused by PFA fixation. To ensure optimal interaction between antigen and antibody, we should make sure that antibody solutions are thoroughly homogenized, and that the blocking solution contains an adequate concentration of Triton in order to permeabilize the nuclear envelope. Altogether, these quality improvement techniques may help optimize the efficacy of parallel PV and NeuN and parallel PV and ankyrin-G staining. These methods can then be used in subsequent

experiments to continue investigating the role of PV interneuron subtype in patterns of PV cell loss observed in FAD neuropathology.

The findings of this study contribute to efforts to fill the gap in knowledge regarding the role of PV and SST interneurons in extracellular A β deposition and plaque aggregation in 5XFAD mice and postmortem samples from patients diagnosed with AD. This study also presents immunohistochemical methods for future studies of PV interneuron density loss by PV cell subtype in 5XFAD, as well as several intriguing questions in light of our results, regarding the interactions between interneurons, A β , plaques, and cell density in AD. Opportunities for further research include investigating: why plaque burden is low on average inside the PV cell in 5XFAD and human tissues; why the PV neuron microenvironment is more conducive to A β and plaque aggregation than the general neuronal population in both 5XFAD and human tissues; why the SST neuron microenvironment is less conducive to A β and plaque aggregation than the general neuronal population; and how levels of neural activation may be related in some way to local aggregation of extracellular A β and plaques.

Empirical study of neurochemical and molecular characteristics unique to the PV microenvironment that contribute to enhanced plaque formation may identify potential targets for therapeutic drugs. It has been demonstrated that aggregation of A β into plaques may be accelerated by interactions between A β and glycosaminoglycans (GAGs) and between A β and acidic phospholipids (McLaurin, Yang, Yip, & Fraser, 2013). It is possible, then, that the microenvironments surrounding PV cells may have high levels of GAGs or acidic phospholipids, and if either is the case, then it could be

possible to decrease A β plaque formation by inhibiting binding of GAGs to A β or by inhibiting the production of acidic phospholipids. So, by identifying agents that accelerate plaque formation near and around PV cells, it is possible to determine how those accelerated processes of plaque formation may be inhibited.

Additionally, identification of any factors within PV cells that prevent accumulation of A β may allow for transfer of those resistance factors to other cells as a means of protection from A β aggregation. It is known, for example, that modification of A β intracellularly by pyroglutamate accelerates accumulation of A β aggregates into plaques (Moon, 2012). It is possible then, that if PV cells possess less pyroglutamate than other cells that are more vulnerable to intracellular A β aggregation, then reducing pyroglutamate in other cells may also make those cells more resistant to intracellular A β aggregation. This theory has not yet undergone extensive empirical investigation, but presents an opportunity for better understanding why PV cells are resistant to intracellular A β aggregation, and thus how other cells may be treated in order to increase resistance to intracellular A β aggregation, as well.

Thus, this study demonstrates that the PV interneuron microenvironment is conducive to extracellular plaque and A β aggregation and that the PV cell is somehow resistant to intracellular A β deposition, effectively identifying the PV microenvironment as a potential source for finding AD drug targets and the PV cell as a potential source for finding potential protective factors against A β aggregation.

Acknowledgements

I would like to thank Dr. Farhan Ali and Dr. Alex Kwan for advising my project and Dr. Jaime Grutzendler for providing human postmortem tissue from Alzheimer's patients. I would also like to thank my parents, friends, and the members of Yale Chi Alpha for their continuous encouragement and moral support.

References

- Ali, F., Baringer, S. L., & Kwan, A. C. (n.d.). Parvalbumin-positive neuron loss and amyloid-beta deposits in the frontal cortex of Alzheimer's disease-related mice. *Unpublished Manuscript*.
- Arendt, T., Bigl, V., Tennstedt, A., & Arendt, A. (1985). Neuronal loss in different parts of the nucleus basalis is related to neuritic plaque formation in cortical target areas in alzheimer's disease. *Neuroscience*, 14(1), 1–14. [https://doi.org/10.1016/0306-4522\(85\)90160-5](https://doi.org/10.1016/0306-4522(85)90160-5)
- Armstrong, R. A. (2015). Original article Laminar distribution of β -amyloid (A β) peptide deposits in the frontal lobe in familial and sporadic Alzheimer's disease. *Folia Neuropathologica*, 1, 15–23. <https://doi.org/10.5114/fn.2015.49970>
- Arnold, S. E., Hyman, B. T., Flory, J., Damasio, A. R., & Van Hoesen, G. W. (1991). The topographical and neuroanatomical distribution of neurofibrillary tangles and neuritic plaques in the cerebral cortex of patients with Alzheimer's disease. *Cerebral Cortex (New York, N.Y.: 1991)*, 1(1), 103–116.
- Brun, A., & Englund, E. (1981). Regional pattern of degeneration in Alzheimer's disease: neuronal loss and histopathological grading. *Histopathology*, 5(5), 549–564.
- Calhoun, M. E., Wiederhold, K.-H., Abramowski, D., Phinney, A. L., Probst, A., Sturchler-Pierrat, C., ... Jucker, M. (1998). Neuron loss in APP transgenic mice. *Nature*, 395(6704), 755–756. <https://doi.org/10.1038/27351>

- Carter, J., & Lippa, C. F. (2001). Beta-amyloid, neuronal death and Alzheimer's disease. *Current Molecular Medicine*, 1(6), 733–737.
- Cras, P., Kawai, M., Lowery, D., Gonzalez-DeWhitt, P., Greenberg, B., & Perry, G. (1991). Senile plaque neurites in Alzheimer disease accumulate amyloid precursor protein. *Proceedings of the National Academy of Sciences of the United States of America*, 88(17), 7552–7556. Retrieved from PubMed. (1652752)
- Eimer, W. A., & Vassar, R. (2013). Neuron loss in the 5XFAD mouse model of Alzheimer's disease correlates with intraneuronal A β 42 accumulation and Caspase-3 activation. *Molecular Neurodegeneration*, 8(2). <https://doi.org/10.1186/1750-1326-8-2>
- Girard, S., Baranger, K., Gauthier, C., Jacquet, M., Bernard, A., Escoffier, G., ... Roman, F. (2013). Evidence for early cognitive impairment related to frontal cortex in the 5XFAD mouse model of Alzheimer's disease. *Journal of Alzheimer's Disease*, 33(3), 781–796. <https://doi.org/10.3233/JAD-2012-120982>
- Govindpani, K., Guzmán, B. C.-F., Vinnakota, C., Waldvogel, H. J., Faull, R. L., & Kwakowsky, A. (2017). Towards a Better Understanding of GABAergic Remodeling in Alzheimer's Disease. *International Journal of Molecular Sciences*, 18(8). <https://doi.org/10.3390/ijms18081813>
- Jawhar, S., Trawicka, A., Jenneckens, C., Bayer, T. A., & Wirths, O. (2012). Motor deficits, neuron loss, and reduced anxiety coinciding with axonal degeneration and intraneuronal A β aggregation in the 5XFAD mouse model of Alzheimer's

- disease. *Neurobiology of Aging*, 33(1), 196.e29-196.e40.
<https://doi.org/10.1016/j.neurobiolaging.2010.05.027>
- Klunk, W. E., Engler, H., Nordberg, A., Wang, Y., Blomqvist, G., Holt, D. P., ... Långström, B. (2004). Imaging brain amyloid in Alzheimer's disease with Pittsburgh Compound-B. *Annals of Neurology*, 55(3), 306–319.
<https://doi.org/10.1002/ana.20009>
- Mann, D. M., Yates, P. O., & Marcyniuk, B. (1985). Correlation between senile plaque and neurofibrillary tangle counts in cerebral cortex and neuronal counts in cortex and subcortical structures in Alzheimer's disease. *Neuroscience Letters*, 56(1), 51–55. [https://doi.org/10.1016/0304-3940\(85\)90439-2](https://doi.org/10.1016/0304-3940(85)90439-2)
- Martinez, V. (2013). Chapter 180 - Somatostatin. In A. J. Kastin (Ed.), *Handbook of Biologically Active Peptides (Second Edition)* (pp. 1320–1329).
<https://doi.org/10.1016/B978-0-12-385095-9.00180-9>
- Masters, C. L., Bateman, R., Blennow, K., Rowe, C. C., Sperling, R. A., & Cummings, J. L. (2015). Alzheimer's disease. *Nature Reviews Disease Primers*, 1(15056). <https://doi.org/10.1038/nrdp.2015.56>
- McLaurin, J., Yang, D.-S., Yip, C. M., & Fraser, P. E. (2000). Review: Modulating Factors in Amyloid- β Fibril Formation. *Journal of Structural Biology*, 130(2), 259–270. <https://doi.org/10.1006/jsbi.2000.4289>
- Molgaard, S., Ulrichsen, M., Boggild, S., Holm, M., Vaegter, C., Nyengaard, J., & Glerup, S. (2014). Immunofluorescent visualization of mouse interneuron

subtypes. *F1000Research*, 3(242).

<https://doi.org/10.12688/f1000research.5349.1>

Moon et al. - 2012 - Intracellular amyloid- β accumulation in calcium-bi.pdf. (n.d.).

Moon, M., Hong, H.-S., Nam, D. W., Baik, S. H., Song, H., Kook, S.-Y., ...

Mook-Jung, I. (2012). Intracellular amyloid- β accumulation in calcium-binding protein-deficient neurons leads to amyloid- β plaque formation in animal model of Alzheimer's disease. *Journal of Alzheimer's Disease*, 29(3), 615–628.

<https://doi.org/10.3233/JAD-2011-111778>

Oakley, H., Cole, S. L., Logan, S., Maus, E., Shao, P., Craft, J., ... Vassar, R.

(2006). Intraneuronal Beta-Amyloid Aggregates, Neurodegeneration, and Neuron Loss in Transgenic Mice with Five Familial Alzheimer's Disease Mutations: Potential Factors in Amyloid Plaque Formation. *The Journal of Neuroscience*, 26(40), 10129–10140.

<https://doi.org/10.1523/JNEUROSCI.1202-06.2006>

Paxinos, G., & Franklin, K. (2012). *Paxinos and Franklin's the mouse brain in stereotaxic coordinates* (4th ed.). Academic Press.

Rowe, C. C., Ng, S., Ackermann, U., Gong, S. J., Pike, K., Savage, G., ...

Villemagne, V. L. (2007). Imaging beta-amyloid burden in aging and dementia. *Neurology*, 68(20), 1718–1725.

<https://doi.org/10.1212/01.wnl.0000261919.22630.ea>

Saiz-Sanchez, D., De la Rosa-Prieto, C., Ubeda-Banon, I., & Martinez-Marcos, A.

(2015). Interneurons, tau and amyloid-b in the piriform cortex in Alzheimer's

disease. *Brain Structure and Function*, 220(4), 2011–2025.

<https://doi.org/10.1007/s00429-014-0771-3>

Saiz-Sanchez, D., Ubeda-Banon, I., De la Rosa-Prieto, C., & 2, A. (2012).

Differential expression of interneuron populations and correlation with amyloid- β deposition in the olfactory cortex of an A β PP/PS1 transgenic mouse model of Alzheimer's disease. *Journal of Alzheimer's Disease*, 31(1), 113–129.

<https://doi.org/10.3233/JAD-2012-111889>

Spires, T. L., & Hyman, B. T. (2005). Transgenic models of Alzheimer's disease:

Learning from animals. *The Journal of the American Society for Experimental NeuroTherapeutics*, 2(3), 423–437. <https://doi.org/10.1602/neurorx.2.3.423>

Takahashi, H., Brasnjevic, I., Rutten, B., Van Der Kolk, N., Perl, D., Bouras, C., ...

Dickstein, D. (2010). Hippocampal interneuron loss in an APP/PS1 double mutant mouse and in Alzheimer's disease. *Brain Structure and Function*, 214(2–3), 145–160. <https://doi.org/10.1007/s00429-010-0242-4>

Taniguchi, H., Lu, J., & Huang, Z. J. (2013). The spatial and temporal origin of

chandelier cells in mouse neocortex. *Science*, 339(6115), 70–74.

<https://doi.org/10.1126/science.1227622>

Troubleshooting and using controls in IHC and ICC | Abcam. (2019). Retrieved April

21, 2019, from

<https://www.abcam.com/protocols/troubleshooting-and-using-controls-in-ihc-and-icc>

- Vargova, G., Vogels, T., Kostecka, Z., & Hromadka, T. (2018a). Inhibitory interneurons in Alzheimer's disease. *Bratislavske Lekarske Listy*, 119(4), 205–209. https://doi.org/10.4149/BLL_2018_038
- Vargova, G., Vogels, T., Kostecka, Z., & Hromadka, T. (2018b). Inhibitory interneurons in Alzheimer's disease. *Bratislava Medical Journal*, 119(04), 205–209. https://doi.org/10.4149/BLL_2018_038
- Yuan, P., Condello, C., Keene, C. D., Wang, Y., Bird, T. D., Paul, S. M., ... Grutzendler, J. (2016). TREM2 haplodeficiency in mice and humans impairs the microglia barrier function leading to decreased amyloid compaction and severe axonal dystrophy. *Neuron*, 90(4), 724–739. <https://doi.org/10.1016/j.neuron.2016.05.003>
- Yuan, P., & Grutzendler, J. (2016). Attenuation of β -amyloid deposition and neurotoxicity by chemogenetic modulation of neural activity. *The Journal of Neuroscience*, 36(2), 632–641. <https://doi.org/10.1523/JNEUROSCI.2531-15.2016>